Cyclotron motion of two Coulombically interacting ion clouds with implications to Fourier-transform ion cyclotron resonance mass spectrometry

Dale W. Mitchell and Richard D. Smith
Department of Chemical Sciences, Pacific Northwest Laboratory, P.O. Box 999, Mail Stop P8-19, Richland, Washington 99352
(Received 27 April 1995)

This work investigates the cyclotron motion of two Coulombically interacting ion clouds with different mass-to-charge ratios. Trap geometry as well as the shape of each ion cloud determines the maximum number of ions that can be confined in a Penning-like ion trap. We consider the two important cases of either spherically or cylindrically shaped ion clouds. These models exhibit the most important space charge effects in Fourier-transform ion cyclotron resonance mass spectrometry including frequency shifts, amplitude and phase modulation, and phase locking. Both positive and negative frequency shifts are possible for spherical ion clouds when their cyclotron radii differ. Due to the Coulombic interaction between ion clouds, both cyclotron-radius and phase modulation occur. This modulation increases inversely to the cyclotron frequency difference. Cyclotron phase locking results when two ion clouds have similar mass-to-charge ratios and a sufficiently large ion population, at which point a mass spectrum shows only a single peak. Spherical ion clouds are usually more likely to phase lock than cylindrically shaped clouds. The phase-locking threshold sets limits on the maximum resolution, mass accuracy, and dynamic range achievable by mass spectrometry. Phase locking is treated in detail and our results are compared to previously published experimental data. The present model quantitatively describes the onset of phase locking as well as the general trends in frequency shifts and measured abundances just before phase locking.

PACS number(s): 46.10.+z, 07.75.+h, 42.60.Fc, 82.80.Ms

I. INTRODUCTION

Fourier-transform ion cyclotron resonance (FT-ICR) mass spectrometry has established itself as the best method for obtaining precise and accurate mass determinations of molecular species extending to the size of large biomolecules [1–9]. Through the combination of FT-ICR with soft ionization techniques including electrospray [9–12] and matrix assisted laser desorption ionization [13–15], the realm of large molecules is accessible, increasing the interest in high resolution measurements and high mass-to-charge (m/q) ratio ions [8,9].

The heart of the instrument is the ICR Penning trap positioned in an ideally homogeneous magnetic field $B\hat{k}$, directed along the z axis of the trap [4,16,17]. The magnetic field and trapping potentials V_t applied on the z electrodes provide radial and axial confinement, respectively. A single m/q ion (also conveniently expressed as m/Z where m is the mass in u and Z is the number of elementary charges per ion) executes a fundamental periodic motion normal to the magnetic field at the cyclotron frequency ω_c:

$$\omega_c = qB/m = ZeB/m \ . \tag{1}$$

An ICR mass spectrometer weighs ions by measuring their cyclotron frequencies. In a cylindrical coordinate system (r,θ,z), positively and negative charged ions rotate in the clockwise $(-\hat{\theta})$ and counterclockwise $(+\hat{\theta})$ directions, respectively. For a quadrupolar trapping potential the z motion is also periodic at a frequency ω_z and the cyclotron frequency is slightly reduced from ω_c to a trapping voltage dependent cyclotron frequency ω_+. In addition, the quadrupolar potential creates a radial electric field resulting in a slow $\vec{E}\times\vec{B}$ drift of the ion around the trap symmetry axis at the magnetron frequency ω_-. The effective cyclotron and magnetron frequencies $\omega_\pm$ are [18]

$$\omega_\pm = \frac{\omega_c}{2}\left[1 \pm \left[1-\frac{2\omega_z^2}{\omega_c^2}\right]^{1/2}\right] . \tag{2}$$

Bound motion is only possible provided $\omega_c > \sqrt{2}\omega_z$ or equivalently $\omega_+ > \omega_-$. In the most basic FT-ICR experiment, an ensemble of typically $\sim 10^3$ to 10^6 ions, consisting of several or perhaps many different m/Z's, is confined symmetrically about the ICR trap center. The cyclotron modes of the individual ions are then excited coherently by rf dipolar excitation at ω_+ to ideally the same cyclotron radius. Each m/Z ion cloud induces an image current with a frequency at ω_+ on the detection electrodes. (An ion cloud is defined here as a coherently moving ion distribution of the same m/Z.) The mass spectrum is easily obtained by the inverse relationship between m/q and cyclotron frequency ω_c, or more precisely by a mass calibration based on Eq. (2) which includes the trapping potential dependence [4,19]. Hence, if the initial ensemble of ions contains two different m/Z's, after cyclotron excitation the trap contains two coherently moving ions clouds.

Detailed discussions of single ion dynamics are in the literature [4,18,20–24]. The equations of motion for a single ion in the presence of a perturbation force $\vec{F}$ are

given in the Appendix. A deeper understanding of space charge effects is required in order to make further improvements in the FT-ICR method [8]. Due to the Coulombic interaction between different m/Z ion clouds, the cyclotron trajectories of the ions are perturbed from circular orbits moving with the cyclotron frequency, resulting in a sometimes dramatic variation from the behavior predicted for a single ion. Phenomena arising from the Coulombic interaction between different m/Z ion clouds, same m/Z ions, or image charge induced on the trap electrodes, are generically referred to as space charge effects. Coulomb induced frequency shifts [25–39], amplitude and phase [40] modulation, and phase locking [41,42] are the most important space charge effects in FT-ICR. The Coulomb interaction between two different m/Z ion clouds excited to some cyclotron radius (not necessarily the same radius) modifies the radial electric field experienced by the ion clouds. The cyclotron frequencies are shifted from their unperturbed values as a result of this space charge induced radial electric field. Since the distance between the ion clouds changes with periodicity $\sim\Delta\omega_c^{-1}$, where $\Delta\omega_c$ is the cyclotron frequency difference, the cyclotron phases are modulated. The cyclotron radii are modulated as well since the mutual $\vec{E}_c\times\vec{B}$ drift between the two ion clouds, where $\vec{E}_c$ is the space charge induced electric field, causes a variation in radius with time. (The ion clouds tend to avoid each other when they get close together.) However, if $\Delta\omega_c$ is small compared to the $\vec{E}_c\times\vec{B}$ drift frequency, the two ion clouds may phase lock, whereby both clouds revolve around one another as well as the trap center. During phase locking, a mass spectrum shows only a single peak, and not two peaks. The primary goal of this work is to elucidate the behavior of these three phenomena through an analysis of simple physical models for space charge effects.

Section II discusses the relationship between trap geometry, ion cloud shape, and ion confinement for an unexcited ion cloud. Section III contains results of theoretical investigations for the dynamics of two interacting ion clouds, each possessing a coherent cyclotron mode. Space charge effects are treated analytically by the models of either two interacting point charges or two infinitely long line charges. The more realistic models of interacting charged spheres and infinitely long charged cylinders are studied by numerical simulations. Included here are the calculated cyclotron frequency shifts and phase-locking thresholds. Implications of cyclotron frequency shifts and phase locking to precision mass spectrometry are discussed. Section IV presents a few concluding remarks.

II. THE UNEXCITED ION CLOUD

An important question concerns the appropriateness of various simple models to describe space charge effects in FT-ICR mass spectrometry. The best approach is probably to follow the dynamics of each ion, but is computationally intensive for a realistic number of ions and does not lend itself to analytical solution. The simplest models [25,26,31,42,43] which retain much of what is known in the FT-ICR excitation and detection process are those which assume that each ion cloud is treated as a point charge, line charge, or finite size distribution which interacts only with ion clouds with a different m/Z. Hence, the Coulomb interaction is included only between different m/Z ion clouds and not between ions in the same ion cloud. Inherent in this class of space charge effect model is the assumption that the individual ion clouds are stable during the ICR detection period. Experimental observations of coherent cyclotron motion lasting longer than 10^6 cyclotron periods demonstrate extraordinary stability for compact ion clouds with an excited cyclotron mode [32,44,45]. The traditional view concerning space charge effects is that if too many ions are confined Coulomb induced frequency shifts, which are position dependent, lead to broadening of the ICR signal [25,26]. However, $\vec{E}_c\times\vec{B}$ drifts, where $\vec{E}_c$ is the radial electric field with the origin at the ion cloud center due to the Coulomb interaction for same m/Z ions within an excited ion cloud, result in a rotation of the ion cloud about the cloud's own symmetry axis, assuming that the ion cloud is a uniform charge density ellipsoid of revolution [46–53]. This internal rotation, which may be thought of as an ion cloud spin, is independent of the single ion magnetron motion, where the latter is due to the radial ICR trap electric field. If the ion cloud is displaced from the trap symmetry axis, the ion cloud now has a nonzero magnetron radius and the ion cloud still has the spin rotation about its own axis of symmetry. This spin rotation has recently been predicted [52] to give the postexcitation ion cloud enhanced cyclotron mode stability against shear, such as may arise from small differences in the cyclotron frequency at different positions in the ion cloud due to field inhomogeneities. Somewhat paradoxically, cloud stability is enhanced at lower magnetic fields and higher charge density within the ion cloud [52]. These dependencies can be understood by noting that the ion cloud spin rotation rate is proportional to E_c and inversely proportional to B.

Radial confinement and z confinement set two basic limits to the total number of ions which can be trapped in an ICR trap [46]. It is also possible to deduce the most appropriate simple physical model for the ion cloud shape from these considerations. In this work we consider two simplified models for the ion cloud distribution, namely, uniform charge density spheres or infinitely long cylinders. The z confinement limit is determined by the condition that the space charge potential at $r=0$ (trap center) is equal to the trapping potential well depth. Consider first the model of an infinitely long uniform charge density cylinder of radius ρ_c, charge per length Nq/L, along the symmetry axis of an infinitely long grounded cylindrical conductor of radius r_w. Solving Poisson's equation (or Gauss's law) gives for the electric potential along the axis ($r=0$) [46]

$$\Phi_0^{\rm cyl}=\frac{Nq}{4\pi\varepsilon_0 L}\left[1+2\ln\frac{r_w}{\rho_c}\right], \tag{3}$$

where N is the total number of ions, each of charge $q=Ze$, in a cylinder L meters long. Similarly, if a uni-

form density spherical charge distribution of radius ρ_c is at the center of a grounded conducting sphere of diameter d, one obtains

$$\Phi_0^{\text{sphere}} = \frac{Nq}{4\pi\varepsilon_0}\left[\frac{3}{2\rho_c} - \frac{1}{r_w}\right] \tag{4}$$

for the space charge potential at the center of the sphere ($r=0$). The condition for z confinement is that the space charge potential is less than the trapping potential well depth. The trapping well depth at the center of a tetragonal or cylindrical ICR trap with trapping potential V_t on the z electrodes and ground on all other electrodes is equal to $V_t(1-D_0)$, where D_0 is a geometric factor. $D_0=\frac{1}{3}$ for a cubic ICR trap and decreases monotonically such that $D_0 \approx 0$ for elongated traps with trap length-to-diameter ratios greater than 2. The z confinement condition is then $\Phi_0 < V_t(1-D_0)$. Combining with Eqs. (3) and (4) for a cylindrical charge distribution (in units of numbers of ions per volt trapping) yields [46]

$$\left[\frac{N}{V_t}\right]^{\text{cyl}} < \frac{4\pi\varepsilon_0 L(1-D_0)}{q}\left[1+2\ln\frac{r_w}{\rho_c}\right]^{-1} \tag{5}$$

and for a spherical charge distribution yields

$$\left[\frac{N}{V_t}\right]^{\text{sphere}} < \frac{4\pi\varepsilon_0(1-D_0)}{q}\left[\frac{3}{2\rho_c} - \frac{1}{r_w}\right]^{-1}. \tag{6}$$

As an example, consider the case of a 5 cm long cubic trap, $\rho_c=0.1$ cm, and $q=e$. For simplicity in the case of cylindrical distributions, we assume that the charge distribution extends the whole trap length such that $L=5$ cm. For these parameters, one obtains $N/V_t < 3\times10^6$ and $N/V_t < 3\times10^5$ V^{-1}, for a cylindrical and spherical charge distribution, respectively. A long cylindrical distribution generates a much smaller space charge potential than a spherical charge distribution for equal radius clouds with the total charge in the sphere equal to the total charge in the cylinder of length $L \gg \rho_c$. As individual ions are added one by one into the trap along the z axis and allowed to cool, the initial charge distribution can be nearly spherical up to the point where a spherical charge distribution is not allowed by z confinement limits. The ion cloud either expands radially or elongates along the ICR trap axis.

The radial dynamics of an ion cloud composed of a species of one specific m/Z in thermal equilibrium is complicated; for simplicity we discuss only the static properties of an unexcited ion cloud located at the trap center [46,47,50,53]. The ion cloud with axis of symmetry collinear with the ICR trap axis and parallel to the magnetic field has a thermal distribution which is identical to a Maxwell-Boltzmann distribution in the frame of reference rotating with frequency ω_r (the ion cloud spin rotation rate due to $\vec{E}\times\vec{B}$ drift) [46,47,50]. This spin rotation is due to the ion cloud's own space charge electric field. Therefore, if the ion cloud is moved off the trap z axis (e.g., given a nonzero magnetron radius), this ion cloud still has spin ω_r about its own symmetry axis with the magnetron motion superimposed. In the limit that ω_z is small compared to the plasma frequency, the distribution tends towards a long cylindrical ion cloud extending the entire length of the ICR trap [46,47,50].

The radial force balance between the Lorentz force, arising from the space charge electric field, the magnetic field, and the centrifugal force for a uniform density cylindrical column of charge rotating about its symmetry axis sets a maximum number density that can be achieved known as the Brillouin limit n_B [46,47,50]. For either an infinitely long cylindrical charge distribution or a cold ion cloud in thermal equilibrium located at the bottom of a Penning trap potential [46–51]

$$n_B = \frac{\varepsilon_0 B^2}{2m}. \tag{7}$$

While the maximum *number* density n_B is charge independent, the maximum *charge* density qn_B is inversely proportional to m/Z. As an example, the maximum achievable number density for a cloud consisting of $m=1000$ u ions in a 1 T magnet is 2.6×10^6 cm^{-3}, regardless of the number of charges carried by each ion. Assuming that the ion cloud is cylindrical with N ions of charge q in a cylinder of L m long, combining Eqs. (7) and (5), then solving for the critical trapping voltage $V_t=V_c$, yields

$$V_c(1-D_0) = \frac{B^2\rho_c^2 q}{32m}\left[1+2\ln\frac{r_w}{\rho_c}\right]. \tag{8}$$

For $V_t < V_c$, the Brillouin limit cannot be exceeded since the trapping potential well depth is too shallow and the ions may remain within the defined cylindrical volume. For $V_t > V_c$, the Brillouin limit is exceeded if the trap is allowed to be completely filled with ions, and the ion cloud expands radially until the density is reduced. V_c predicted by Eq. (8) is actually an underestimate since ions leak out the trap along the z axis due to thermal motion. The maximum number of ions which can be confined is likely smaller than predicted by Eq. (5). If ρ_c is chosen equal to the radius of the ionizing electron beam or the radius of the beam of externally generated ions entering the trap, then Eq. (8) gives an estimate of the trapping potential V_c or trapping well depth $V_c(1-D_0)$ above which the ion cloud must expand radially if the trap is filled to capacity with ions. It is well recognized [8] that at high trapping potentials and high m/Z the FT-ICR performance is degraded, particularly when too many ions are confined. Equation (8) gives a possible explanation. Since V_c is inversely proportional to m/Z, it is easier to confine lower m/Z ions in a small diameter column than high m/Z ions. As an example consider the case of a cubic ICR trap ($D_0=\frac{1}{3}$), $r_w=2.5$ cm, $m/Z=100$ u, and $B=1$ T. Also, the ions are assumed to be generated along the z axis by electron impact ionization within the trap by an electron beam of radius $\rho_c=0.1$ cm. Using Eq. (8), the critical well depth is 0.63 V and $V_c=0.94$ V. For $V_t > V_c$ and the trap filled to capacity with ions, the ion cloud has to expand such that $\rho_c > 0.1$ cm. For a deep potential well such that $V_t > V_c$, and where ions are continually cooled towards the trap

center, the ion cloud reaches the Brillouin limit before spreading sufficiently to reach the z electrodes. Once the Brillouin limit is reached and ions are continually introduced into the trap, the plasma maintains a constant aspect ratio, expanding both radially and axially until it contacts one of the electrodes [53].

Previous experimental work [30,31] demonstrates that modeling space charge effects in FT-ICR experiments by assuming cylindrical (or line charge) distributions provides a more realistic description in simulating practical experimental conditions than assuming spherical (or point charge) charge distributions. In one experiment employing a slightly elongated cylindrical ICR trap, a single m/Z ion cloud is excited to a coherent cyclotron radius leaving all other m/Z ions at the trap center [30]. By measuring the cyclotron frequency shift as a function of cyclotron radius, much better correlation is found between experiment and model calculations for a line charge distribution, compared to a point distribution. In a different approach, which includes image charge effects, very good agreement is found between measured cyclotron frequency shifts for two different m/Z ion clouds excited to the same cyclotron radii with theoretical calculations based on assuming that each ion cloud is an infinitely long line charge [31]. One therefore expects that simplified theoretical models based on cylindrical charge distributions are more appropriate to the FT-ICR experiment than approaches based on using spherical (or point charge) distributions. In addition, trap geometries which are either elongated [54] along the z axis or have grounded screens [55] in front of the z electrodes (end caps) have sufficiently flat z confinement potentials such that the ion cloud is approximately cylindrical in shape with $L \gg \rho_c$.

Predicted space charge effects tend to be more pronounced for spherical than for cylindrical ion clouds of the same diameter and total charge. The phenomenon of phase locking is much more sensitive to the shape (and hence interaction potential) of the ion clouds than frequency shifts. Phase locking occurs in spherically shaped ion clouds with far fewer ions than cylindrically shaped ion clouds of the same diameter. Quantitative agreement between the present theory and previously published experimental data is obtained only for a cylindrical charge distribution with a nonzero diameter.

III. CYCLOTRON DYNAMICS

Simple physical models are employed to investigate the dominant behavior associated with space charge effects in FT-ICR mass spectrometry. While these models are too complex to yield exact analytical solutions, approximate results are still obtainable. For a more realistic model, the finite size of ion clouds is included in most of the numerical simulations. For simplicity, the analysis is restricted to two-dimensional motion in the x-y plane.

We shall derive the cyclotron equations of motion for line and point charge models, beginning first with those equations for the line charge model. As variables (see Fig. 1), we choose the cyclotron radii (R_1 and R_2), and the cyclotron phases (β_1 and β_2), where the subscripts

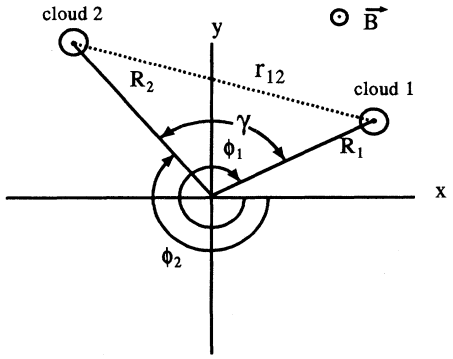

FIG. 1. Geometry for two ion clouds in the $z=0$ plane. Ion cloud j ($j=1,2$) has cyclotron radius and phase equal to R_j and ϕ_j (where $\phi_j=\omega_{+j}t+\beta_j$), respectively. The magnetron radii equal zero. In the numerical simulations the magnetron motion is included as well as the cyclotron motion. Each ion cloud has a radius equal to ρ_c.

denote ion clouds 1 and 2, respectively. Magnetron motion is not included in the analytical equations, but is included explicitly in the numerical simulations. The electric field for an infinitely long, uniform density cylinder of radius ρ_c a distance r from the center is

$$E=\begin{cases}\left[\dfrac{Nq}{2\pi\varepsilon_0\rho_c^2 L}\right]r, & r<\rho_c \quad (9a)\\ \left[\dfrac{Nq}{2\pi\varepsilon_0 L}\right]\dfrac{1}{r}, & r>\rho_c\ , \quad (9b)\end{cases}$$

where q is the charge ($q=Ze$) of one ion and N is the total number of ions contained in a segment of the cylinder a length L m long. For a line charge, $\rho_c \to 0$; then Eq. (9b) is the radial electric field for all values of r. Using Eqs. (9b) and (A3), the amplitude-phase equations of motion describing the time dependence of the cyclotron radii and phases of two Coulombically interacting line charges is (neglecting image charge effects and magnetron motion)

$$\dot{R}_1=\left[\frac{+q_2N_2R_2}{2\pi\varepsilon_0BLr_{12}^2}\right]\sin(\gamma)\ ,$$
$$\dot{R}_2=\left[\frac{-q_1N_1R_1}{2\pi\varepsilon_0BLr_{12}^2}\right]\sin(\gamma)\ , \quad (10a)$$

$$\dot{\beta}_1=\left[\frac{-q_2N_2}{2\pi\varepsilon_0BLr_{12}^2}\right]\left[1-\frac{R_2}{R_1}\cos(\gamma)\right]\ ,$$
$$\dot{\beta}_2=\left[\frac{-q_1N_1}{2\pi\varepsilon_0BLr_{12}^2}\right]\left[1-\frac{R_1}{R_2}\cos(\gamma)\right]\ , \quad (10b)$$

where R_j, β_j, and q_jN_j/L are the cyclotron radius, cyclotron phase, and line charge density of the jth line charge ($j=1,2$), respectively. Also γ and r_{12} are the instantaneous angular separation and distance between the two line charges, given by

$$\gamma=(\omega_{c1}-\omega_{c2})t+\beta_1-\beta_2 , \tag{11}$$

$$r_{12}^2=R_1^2+R_2^2-2R_1R_2\cos(\gamma) . \tag{12}$$

In Eq. (10) the approximation $\omega_+-\omega_-\approx\omega_c$ has been made, which is accurate provided $\omega_+\gg\omega_z\gg\omega_-$. Neglecting magnetron motion (alternatively called diocotron motion [46,47,50]) is valid under most conditions provided that the initial magnetron radius is small compared to the cyclotron radius and that the frequencies ω_{+1} and ω_{+2} do not satisfy the special commensurability condition $\omega_{+2}/\omega_{+1}=\frac{1}{2},\frac{2}{3},\ldots,n/(n+1),\ldots$ (where n is an integer) [56]. This latter case is unimportant for nearly all parameters (see below).

For completeness, the cyclotron equations of motion for the point charge model are now presented. The electric field for a uniform density sphere of radius ρ_c a distance r from the sphere's center is

$$E=\begin{cases}\left[\dfrac{Nq}{4\pi\varepsilon_0\rho_c^3}\right]r, & r<\rho_c \quad (13a)\\ \left[\dfrac{Nq}{4\pi\varepsilon_0}\right]\dfrac{1}{r^2}, & r>\rho_c , \quad (13b)\end{cases}$$

where N is the total number of ions of charge q coulombs inside the uniformly charged sphere of radius ρ_c. The electric field inside the charge distribution is proportional to r, which is the same dependence as for the cylindrical charge distribution. In general, a uniform charge density ellipsoid of revolution has a radial electric field which is proportional to r [34,47,50]. However, outside the charge distribution the electric field has a radial dependence that varies with ion cloud geometry (e.g., r^{-1} and r^{-2} for cylindrical or spherical clouds). The cyclotron equations of motion for the point charge model ($\rho_c=0$) in amplitude-phase representation are

$$\begin{aligned}\dot{R}_1&=\left[\frac{+q_2N_2R_2}{4\pi\varepsilon_0Br_{12}^3}\right]\sin(\gamma) ,\\ \dot{R}_2&=\left[\frac{-q_1N_1R_1}{4\pi\varepsilon_0Br_{12}^3}\right]\sin(\gamma) ,\end{aligned} \tag{14a}$$

$$\begin{aligned}\dot{\beta}_1&=\left[\frac{-q_2N_2}{4\pi\varepsilon_0Br_{12}^3}\right]\left[1-\frac{R_2}{R_1}\cos(\gamma)\right] ,\\ \dot{\beta}_2&=\left[\frac{-q_1N_1}{4\pi\varepsilon_0Br_{12}^3}\right]\left[1-\frac{R_1}{R_2}\cos(\gamma)\right] ,\end{aligned} \tag{14b}$$

where all variables are defined as for the line charge model. While we have neglected magnetron motion and used the approximation $\omega_+-\omega_-\approx\omega_c$ in deriving Eqs. (10) and (14), these assumptions are not made in the numerical simulations.

The most important phenomena predicted by the simple physical models employed here are cyclotron frequency shifts, amplitude and phase modulations, and phase locking. The Coulomb interaction between two different m/Z ion clouds perturbs the radial electric field experienced by the ion clouds, resulting in a shift from the unperturbed (quadrupolar) cyclotron frequency [25,26]. Since the distance between the ion cloud, varies with a periodicity $\sim 1/\Delta\omega_c$, the cyclotron phases and radii are both modulated. The radii are modulated due to their mutual $\vec{E}_c\times\vec{B}$ drifts, where $\vec{E}_c$ is the Coulomb electric field. The ion clouds tend to avoid each other when they get closer together, as one would expect. However, if $\Delta\omega_c$ is small compared to the $\vec{E}_c\times\vec{B}$ drift frequency, the two clouds may phase lock, whereby both clouds revolve around one another as well as the trap center. Upon phase locking, a mass spectrum shows only a single peak, not two peaks. All of these behaviors are contained in the cyclotron equations of motion, Eqs. (10) and (14).

A. Cyclotron frequency shifts

Frequency shifts for the line charge and point charge models are now derived from Eqs. (10b) and (14b) by the method of averaging [23]. Averaging is applicable provided the cyclotron frequencies are sufficiently different such that $\Delta\omega_c\tau\gg 2\pi$, where τ is the observation time. If $\Delta\omega_c\tau\gg 2\pi$, then γ is fast varying with respect to the time variation of β_1 and β_2. To demonstrate how frequency shifts are obtained one should recall that the x and y positions of the cyclotron position for the jth ion are

$$\begin{aligned}x_j(t)&=R_j\cos(\omega_{cj}t+\beta_j) ,\\ y_j(t)&=-R_j\sin(\omega_{cj}t+\beta_j) .\end{aligned} \tag{15}$$

If the Coulomb interaction is neglected, R_j and β_j are constants of motion. However, due to Coulomb interactions from all other m/Z ion clouds, R_j and β_j are time dependent. With the method of averaging one replaces the right-hand sides of Eqs. (10) and (14) by their average over the individual phases. This is equivalent to averaging over γ from 0 to 2π. We define the average of any function F by $\langle F\rangle$,

$$\langle F\rangle=\frac{1}{2\pi}\int_0^{2\pi}F\,d\gamma . \tag{16}$$

In particular, the cyclotron frequency shift $\delta\omega_c$ is given by $\delta\omega_c=\langle\dot{\beta}\rangle$. Applying Eq. (16) to Eq. (10), one finds that $\langle\dot{R}_j\rangle=0$ (implying that the cyclotron radii are approximate constants of motion) and that in general $\langle\dot{\beta}_j\rangle\neq 0$. Considering first the line charge model [Eq. (10b)] we find that

$$\delta\omega_{c1}=\begin{cases}\dfrac{-q_2N_2}{2\pi\varepsilon_0BLR_1^2}, & R_2<R_1 \quad (17a)\\ 0, & R_2>R_1 \quad (17b)\\ \dfrac{-q_2N_2}{4\pi\varepsilon_0BLR_1^2}, & R_2=R_1 . \quad (17c)\end{cases}$$

$\delta\omega_{c2}$ is obtained from Eq. (17) by interchanging subscripts 1 and 2. The line charge model predicts that a line charge which has a smaller cyclotron radius than another line charge should experience no cyclotron frequency shift from the larger cyclotron radius line charge.

This result may be understood by noting that the frequency shifts arise from the radial component of the Coulomb electric field. As shown in the Appendix the cyclotron radius and phase equations can be given as (assuming $\omega_+ - \omega_- \approx \omega_c$)

$$\dot{R}_+ = \frac{-F_\theta}{qB} , \qquad \dot{\beta}_+ = \frac{-F_r}{R_+ qB} . \tag{18}$$

F_θ and F_r are the azimuthal and radial components of the Coulomb force, respectively. By averaging over γ, the original problem involving a time-dependent Coulomb force is replaced by a new problem, namely, two interacting charged cylindrical shells. Through averaging, the Coulomb force is smeared over an infinitely long cylindrical shell with a radius equal to the cyclotron radius. For this situation, Gauss's law shows that the inner cylinder experiences no force from the outer cylinder, while the outer cylinder experiences the same radial force from the inner line charge as if the line charge were located at the origin. The frequency shifts are independent of the position of the perturbing line charges. Furthermore, symmetry shows that $F_\theta = 0$ and that the Coulomb force is purely radial for the problem of concentric infinitely long charged cylindrical shells.

When $R_1 = R_2$, the cyclotron frequencies of both line charges are shifted to lower frequencies for positively charged ions. This equation has previously been derived by Gorshkov, Marshall, and Nikolaev [31] who considered just the special case where $R_1 = R_2$. While image charges are neglected in the present analysis, the high symmetry of the line charge model allows a simple solution for the special case of a grounded infinitely long cylinder. Gorshkov, Marshall, and Nikolaev [31] have derived the image charge induced cyclotron frequency shift for two infinitely long line charges with equal cyclotron radius in a grounded cylinder. This result is also applicable to the case of arbitrary cyclotron radius which follows from Eq. (17b).

Applying the averaging method [23] to the simple point charge model yields $\langle \dot{R}_j \rangle = 0$, which shows that the cyclotron radii are approximate constants of motion. The integral of the right-hand sides of Eq. (14) over γ while keeping R_1 and R_2 constant does not have a simple solution, and is singular when the two cyclotron radii are equal. This problem is resolved either by allowing the cyclotron radii to vary with time (since the point charges tend to avoid each other due to their Coulomb interaction) or by replacing the point charge model with a spherical charge model [26]. In this latter case, the Coulomb force is zero when the ion clouds completely overlap. Finite size effects are included in the numerical simulations. However, accurate analytical results for frequency shifts are still possible in the form of power series for the special cases when $R_1 > R_2$ or $R_1 < R_2$ by expanding r_{12}^3 in the denominator and integrating term by term. By averaging, the cyclotron frequency shift for the case $R_1 > R_2$ is

$$\delta\omega_{c1} \approx \frac{-q_2 N_2}{4\pi\varepsilon_0 B R_1^3} \left[1 + \frac{3}{4}\left[\frac{R_2}{R_1}\right]^2 + \frac{45}{64}\left[\frac{R_2}{R_1}\right]^4 + \frac{89}{128}\left[\frac{R_2}{R_1}\right]^6 + \cdots \right] . \tag{19a}$$

Similarly, the case $R_1 < R_2$ yields

$$\delta\omega_{c1} \approx \frac{+q_2 N_2}{4\pi\varepsilon_0 B R_2^3} \left[\frac{1}{2} + \frac{9}{16}\left[\frac{R_1}{R_2}\right]^2 + \frac{75}{128}\left[\frac{R_1}{R_2}\right]^4 + \frac{1225}{2048}\left[\frac{R_1}{R_2}\right]^6 + \cdots \right] . \tag{19b}$$

Averaging predicts that both positive and negative frequency shifts are possible for the simple point charge model depending upon whether R_2 is either greater or smaller than R_1. Contrary to previous works [25,26,30,32–34,37] which predict only negative shifts we find that both positive and negative frequency shifts are possible for the point charge model. These predictions are verified by numerical simulations (see below). The frequency shifts for both line charge and point charge models are m/Z independent, proportional to the total charge in the other ion cloud, and inversely proportional to the magnetic field strength. The analytical frequency shifts are now compared with exact frequency shifts calculated from numerical trajectory calculations.

Numerically, we describe the position of each m/Z ion cloud by

$$x_j(t) = R_j \cos(\omega_{+j} t + \beta_j) + x_{mj} , \qquad y_j(t) = -R_j \sin(\omega_{+j} t + \beta_j) + y_{mj} , \tag{20}$$

where R_j, β_j, x_{mj}, and y_{mj} are the cyclotron radius, cyclotron phase, magnetron x position, and magnetron y position of the jth ion cloud, respectively. These variables are directly obtained by numerical integration of the amplitude-phase equations of motion [Eq. (A3)] for the cyclotron dynamics and the magnetron position equations of motion [Eq. (A8)] for the magnetron dynamics. The entire system of simultaneous first-order differential equations (4× number of ion clouds) is integrated including explicitly the Coulomb interaction.

The numerical integration method used is the first-order Cromer-Euler method [57,58] (also called the last point approximation) which is a simple and absolutely stable algorithm. A constant time-step size [typically $\sim(10^{-4}-10^{-3})\Delta\omega_c^{-1}$ with even smaller time steps for phase-locked ion clouds] is employed, whose adequacy is checked against identical simulations with smaller time steps. Since the differential equations integrate directly the cyclotron radii, cyclotron phases, and magnetron positions, all of which vary slowly in comparison to $\omega_{+j} t$, relatively larger time steps can be used in the present work compared to schemes which directly integrate the equations of motion in Cartesian coordinates in the laboratory frame of reference. We emphasize that any analytical theory must be compared to the exact numerical results.

In most of the numerical simulations, the ion clouds are represented by uniform density infinitely long cylindrical ion clouds or spherical ion clouds. As described earlier, the finite diameter of the spheres or cylinders is taken into account by scaling the point charge model or line charge model interaction force by $(r_{12}/2\rho_c)^3$ or $(r_{12}/2\rho_c)^2$, respectively, when the ion clouds overlap. For separated (nonoverlapping) ion clouds, the usual point charge or line charge forces are used without scaling. This form of scaling for overlapping ion clouds assures that the interaction force is zero for completely overlapped ion clouds and increases linearly with separation distance up to the point $(r_{12}=2\rho_c)$ where the ion clouds are just touching. This form of interaction for overlapping ion clouds is most appropriate for uniform density clouds with circular cross section. For this class of ion clouds, symmetry arguments demonstrate that the interaction force is zero for complete overlap and increases linearly with separation for small separation distances [59]. The numerical calculations of Chen and Comisarow [26] for the interaction force between two charged disks and Hendrickson, Beu, and Laude [40] for their split charge model show that the force is rigorously zero for complete overlap and also that the linear force approximation for overlapping distributions is reasonable.

In all of the numerical calculations, except where noted, we use $N_1=N_2$, $B=1$ T, $L=5$ cm, $q_1=q_2=e$, and $\rho_c=0.1$ cm. For initial conditions the initial cyclotron radii and magnetron radii for both ion clouds are set equal to 1.0 cm and zero, respectively.

Figure 2 presents results of numerical simulations for the cylindrical charge model. In these simulations, $m_1=70$ u and $m_2=100$ u and the number of ions in each cylinder is varied from 10^4 to 10^6. Only the results for β_1 and R_1 are plotted since the magnetron radii did not vary significantly from zero. In addition, β_2 looks very similar to β_1. While $R_1(t)$ oscillates slightly above the initial radius value, $R_2(t)$ oscillates below. Since the magnetron radius does not change much from its initial value (zero), we expect the numerical simulations to agree very well with predictions based on Eq. (10). First of all, the cyclotron radii Eqs. (10a) or (14a) can be combined and then integrated to yield

$$q_1N_1R_1^2+q_2N_2R_2^2=C\ . \tag{21}$$

C is a constant of motion proportional to the canonical angular momentum about the z axis. Since $q_1N_1=q_2N_2$, by Eq. (21), $R_1^2+R_2^2$ is constant. Hence, $R_1(t)$ and $R_2(t)$ are not independent. As R_1 increases, R_2 decreases. Most importantly, Fig. 2(b) shows that R_1 and R_2 do not deviate much from their initial values, less than 0.5% for 10^6 ions. This agrees well with the analytical prediction that the cyclotron radii are approximate constants of motion for incommensurate frequencies and $\Delta\omega_c\tau=62\gg2\pi$, for the conditions used.

The linear variation of β_1 with time has a simple physical interpretation. As can be seen from Eq. (20), a frequency shift away from ω_{+j} corresponds to a linear variation of β_j with time [23]. The cyclotron frequency shift is equal to the slope of a linear variation in β_j as a function of time. This numerical method has been used successfully in studies concerning the effects of nonquadrupolar trapping potentials and inhomogeneous magnetic fields on single ion motion [60,61]. We shall use this method for calculating frequency shifts, numerically. From Fig. 2(a) the cyclotron frequency shift $\delta\omega_c$ is negative.

Figure 3 presents plots of frequency shifts predicted from numerical simulations for the spherical and cylindrical charge models (solid lines) and from the analytical results for the point [Eq. (19)] and line charge [Eq. (17)] models (dashed), respectively. In these calculations, $N_1=N_2=5\times10^4$ ions, $R_1(t=0)=1.0$ cm, while $R_2(t=0)$ is varied from 0.1 to 1.0 cm. All other parameters are the same as used in Fig. 2. The analytical and numerical results are in very good agreement for $R_{20}<0.8$ cm. When $0.8<R_{20}<1.2$ cm, the ion clouds partially overlap since $\rho_c=0.1$ cm. The analytical and numerical results differ for overlapping ion clouds since the analytical results are derived for $\rho_c=0$, i.e., the point charge and line charge models. In general, very good agreement is found for the case of nonoverlapping ion clouds. In particular, the numerical simulations agree

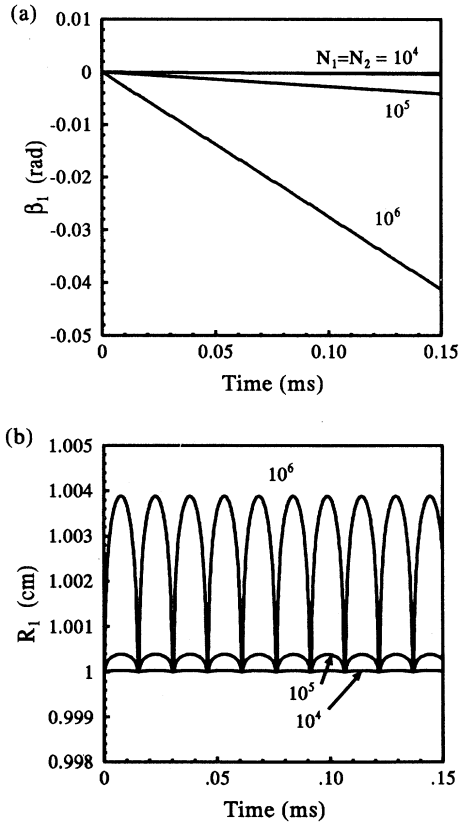

FIG. 2. Numerical simulations of two cylindrical ion clouds at three different ion numbers. (a) β_1 versus time. β_2 (not shown) is nearly identical to β_1. (b) R_1 and R_2 are related by Eq. (21). (Conditions include $m_1=70$ u, $m_2=100$ u, $N_1=N_2$, $B=1$ T, $L=5$ cm, $\rho_c=0.1$ cm, $q_1=q_2=e$, $V_t=0$ V, $R_{10}=R_{20}=1$ cm, $\beta_{10}=\beta_{20}=0$ rad, and zero initial magnetron radii.)

with the prediction that a spherical ion cloud with a cyclotron radius smaller than a second spherical ion cloud experiences a positive frequency shift from the second ion cloud. In Fig. 3(b) the solid square is the analytical frequency shift predicted from Eq. (17c) for the special case $R_1=R_2$ and agrees surprisingly well with the numerical simulations. When $R_{10}=R_{20}$, the numerical simulations for the cylindrical charge and spherical charge models predict negative frequency shifts for both ion clouds.

B. Implications for FT-ICR mass calibration

One of the earliest theories for explaining space charge induced frequency shifts in ICR traps is the model of Jefferies, Barlow, and Dunn (JBD) [34]. In that work the known electric field "inside" a uniformly charged ellipsoid is used to calculate the shifted cyclotron frequency. The radial electric field inside a uniformly charged ellipsoid is proportional to r, the normal distance from the cloud center. The JBD model is valid for the conditions for which it was originally derived but is not completely applicable to typical FT-ICR conditions. In most FT-ICR experiments the ion clouds are not always overlapping and the radial electric field "outside" the ellipsoid is of particular interest. The radial dependence of the electric field outside the ion cloud is different from that inside. For example, uniformly charged spheres and infinitely long cylinders have radial fields proportional to r^{-2} and r^{-1}, respectively, outside of the distributions, compared to simply r inside. The different forms of the interaction outside compared to inside lead to qualitatively different results for the frequency shifts. Earlier work [25] has discussed the inadequacy of the JBD model to properly explain the FT-ICR experiment. They point out that while this model is appropriate for traditional ICR experiments where a single m/Z is excited subjected to the Coulomb interaction of all other m/Z ions remaining at the trap center, in FT-ICR all m/Z ions are simultaneously excited to ideally the same cyclotron radius whose cyclotron frequencies are detected subsequent to excitation. The radial dependence of the Coulomb induced electric field used in the JBD model is also inappropriate to the FT-ICR experiment. The resonance frequencies at which the ions are excited within the initial unexcited charge distribution are correctly explained within the JBD model; however, it incorrectly describes the detected cyclotron frequencies of spatially separated ion clouds after the excitation event.

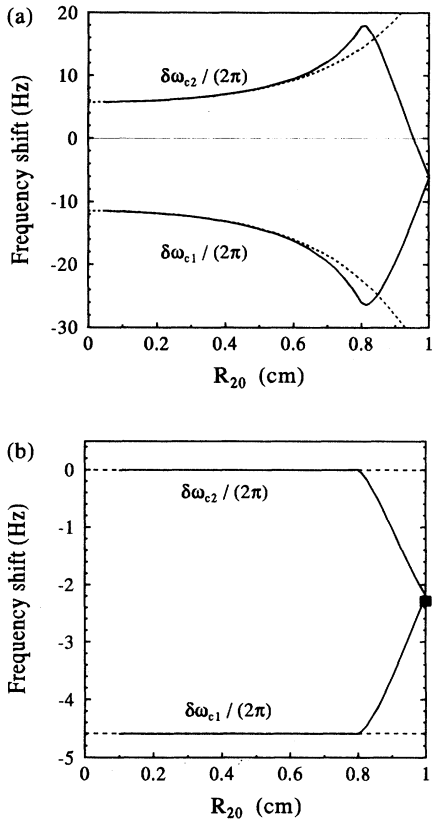

FIG. 3. Analytical (broken lines) and numerical (solid lines) frequency shifts. (a) Analytical point charge model, Eq. (19), frequency shifts compared to numerical simulations using spherical ion clouds ($\rho_c=0.1$ cm). (b) Analytical line charge model, Eq. (17), frequency shifts compared to numerical simulations using cylindrical ion clouds ($\rho_c=0.1$ cm, $L=5$ cm). (The initial cyclotron radius $R_{10}=1$ cm, while R_{20} is varied. $N_1=N_2=50\times10^3$ ions. All other conditions are the same as given in Fig. 2.)

The JBD model [34] has become a standard for developing FT-ICR mass calibration laws which include space charge effects. In fact, Ledford, Rempel, and Gross [19] have shown that this approach works quite well, accounting for approximately 70% of the space charge effects in their experiments. However, we have presented arguments questioning the applicability of the JBD model. The standard FT-ICR mass calibration law is obtained by solving Eq. (2) for m/Z, leading to [19]

$$\frac{m}{Z}=\frac{c_1}{\omega_+}+\frac{c_2}{\omega_+^2}\ , \tag{22}$$

where c_1 and c_2 are calibration constants which are empirically determined by fitting Eq. (22) to known m/Z's and experimentally measured ω_+ values. Theoretically, c_1 is the magnetic field strength while c_2 depends linearly on the trapping potential V_t. This form of calibration is unaltered if the JBD model [34] is used to describe space charge effects since for this case the radial dependence of the Coulomb electric field is identical to the radial dependence of the trapping electric field. With space charge effects included by use of the JBD model, the mass calibration law is independent of cyclotron radius.

We now derive a different mass calibration equation based on the frequency shifts appropriate for FT-ICR. From Eqs. (17) and (19) the Coulomb induced frequency shifts depend on cyclotron radius (the JBD model shifts do not) and are m/Z independent. For this case, one can then show that the calibration is

$$\frac{m}{Z}=\frac{c_1}{(\omega_+-\delta\omega_c)}+\frac{c_2}{(\omega_+-\delta\omega_c)^2}\ , \tag{23}$$

where ω_+ is the measured cyclotron frequency, and c_1, c_2, and $\delta\omega_c$ are calibration constants. In particular, $\delta\omega_c$ is the cyclotron radius dependent, m/Z independent Coulomb induced frequency shift. Since $\delta\omega_c \ll \omega_+$, we expand the denominator in Eq. (23), retaining terms up to $O(\omega_+^{-2})$,

$$\frac{m}{Z} \cong \frac{c_1}{\omega_+} + \frac{c_2^*}{\omega_+^2} + O(\omega_+^{-3}) , \tag{24}$$

where $c_2^* = c_2 + c_1 \delta\omega_c$ is a calibration constant. Equation (24) is in the same form as the standard mass calibration. Just because a mass calibration relation based on the JBD model is in good agreement with experiment at a fixed cyclotron radius does not prove that this model is the correct description of space charge effects in FT-ICR. The work of Ledford, Rempel, and Gross [19] was done at a fixed cyclotron radius in which case Eqs. (22) and (24) predict nearly identical results. At a fixed cyclotron radius, the mass calibration is basically independent of the space charge model. Only at varying cyclotron radii do model differences become significant.

C. Commensurate frequencies

When a certain commensurability condition defined by

$$\frac{\omega_{+2}}{\omega_{+1}} = \frac{n}{n+1} \quad (n = 1, 2, \ldots) \tag{25}$$

is satisfied between the two ion clouds, the possibility of internal resonance exists, which causes the ion cloud's mode amplitudes and phases to modulate on a long time scale. Peurrung and Kouzes [56] were the first to recognize this class of internal resonance by numerical simulations on spherical ion clouds. They assumed that $\omega_z = 0$ in which case $\omega_{+2}/\omega_{+1} = \omega_{c2}/\omega_{c1}$. It turns out that, since $\omega_{+2}/\omega_{+1} \neq \omega_{c2}/\omega_{c1}$ exactly in actual experiments, this class of resonance is probably not very important in most experiments. Under most experimental conditions these resonances are likely avoided.

The commensurability condition Eq. (25) can be understood by considering that two ion clouds with the same cyclotron radius and zero magnetron radius pass each other at the same position in the x-y plane only when Eq. (25) is satisfied. Thus in this simplified model the ion clouds, through their Coulombic interaction, introduce a periodic driving force on a long time scale. We find that magnetron motion is critical for this phenomenon since numerical integration of either Eqs. (10) or (14), which neglect magnetron motion, does not show any commensurate resonance effects.

Figure 4 displays results of numerical simulations (including magnetron motion) for the strongest resonance ($n = 1$) using cylindrical ion clouds with $m_1/Z = 50$ u and $m_2/Z = 100$ u. The conditions include $B = 1$ T, $N_1 = N_2 = 50 \times 10^3$, and $V_t = 0$. The ion clouds initially have equal cyclotron radii (1 cm) and are π out of phase. Figure 4(a) shows the time dependence of the cyclotron and magnetron radii while Fig. 4(b) plots the cyclotron phases. This resonance, as with all others satisfying Eq. (25), shows a strong coupling between cyclotron and magnetron modes over very long time scales. The modulation period is approximately 11×10^3 cyclotron periods of the slower ion cloud. The cyclotron phases, while showing slight modulation, still produce negative and approximately equal frequency shifts on average over the observation time.

Figure 5 plots maximum relative variations in R_1 as a function of $\omega_{c2}/\omega_{c1} = m_1/m_2$ taken from numerical calculations of 12×10^3 different values of m_1/m_2 ranging from 0.4 to almost 1. The lowest order (smallest n) resonances are the strongest, resulting in significant variations in the cyclotron radius. The resonance peaks in Fig. 5 do not accurately represent the true peak heights due to the extreme narrowness of these resonances and the discrete numerical sampling.

The baseline rise of ΔR_1, shown in Fig. 5(b), is due to the resonance $\Delta\omega_c = 0$. This additional resonance, which is contained in Eqs. (10) and (14), is not related to either magnetron motion or the commensurability condition Eq. (25). When $\Delta\omega_c \approx 0$, then $\Delta\omega_c \tau \approx 0$ and averaging the cyclotron equations of motion over γ is not allowed. The $\Delta\omega_c = 0$ resonance is responsible for most of the modula-

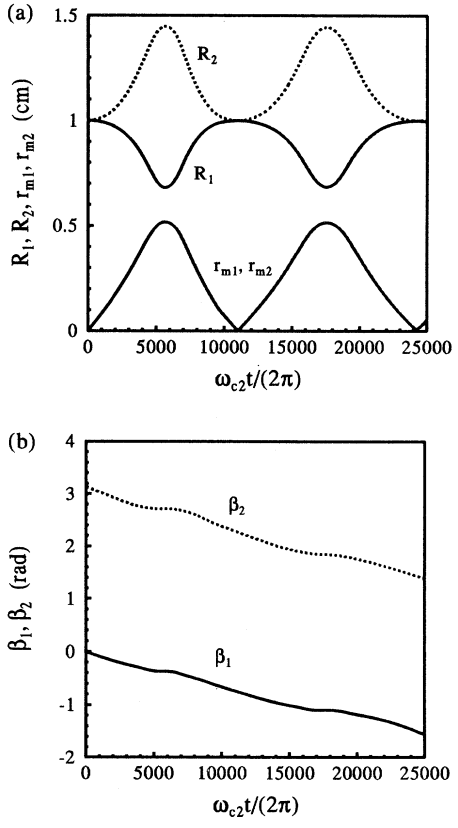

FIG. 4. Numerical simulations of two cylindrical ion clouds at the 1:2 ($n = 1$) resonance. (a) The time evolution of the cyclotron radii R_j and magnetron radii r_{mj} of the two ion clouds. The total canonical angular momentum which is proportional to $\sum_j q_j N_j (r_{mj}^2 - R_j^2)$ is conserved. (b) The time dependence of the cyclotron phases β_j. ($N_1 = N_2 = 50 \times 10^3$, $m_1 = 50$ u, $m_2 = 100$ u, $\beta_{10} = 0$, $\beta_{20} = \pi$, $R_{10} = R_{20} = 1$ cm, $r_{mj}(t=0) = 0$, $B = 1$ T, $L = 5$ cm, $q_1 = q_2 = e$, $\rho_c = 0.1$ cm, and $V_t = 0$ V.)

tion effects [40] and phase-locking [41,42] phenomena observed in FT-ICR experiments.

In order to ascertain the possible importance of resonances satisfying Eqs. (25) we have done numerical simulations which show the dependence of these resonances on trapping voltage, magnetic field strength and resonance order n. Figure 5(b) demonstrates that higher values of n are not important since their effect on R_1 is small and that the $\Delta\omega_c=0$ (phase-locking) resonance dominates the dynamics for $m_1/m_2>0.99$. Therefore we concentrate on the importance of low order resonances. Maximum relative changes in R_1 for ion motion in a cubic Penning trap for three different values of V_t are shown in Fig. 6. At $V_t=0$ V, the resonance is centered near $m_1/m_2=0.5$, while a slight increase in V_t to 0.5 V completely moves the resonance to a higher value of m_1/m_2. This is possibly experimentally significant. Since increasingly important FT-ICR experiments involve isotopic contributions or multiply charged species, the condition $\omega_{c2}/\omega_{c1}=n/(n+1)$ is always satisfied for some particular value of n. In particular, if the two species are singly and doubly charged ions then the dominant $n=1$ resonance exists. However, these resonances are usually extremely narrow and the true commensurability Eq. (25) is normally not exactly satisfied. In addition the higher order resonances (high n values) are not very significant for the conditions shown in Fig. 5. Finally, Fig. 7 presents maximum relative variations in R_1 as a function of magnetic field strength B for two different resonances ($n=1$ and 9). As expected, the $n=1$ resonance is stronger than the $n=9$ resonance. The effect of the magnetic field is to broaden the resonance and increase its magnitude at lower field strength. An estimate of the parameter dependencies on the resonance based on Eq. (10a) shows that the resonance strength is proportional to $N/(BL)$. The modulation amplitude is proportional to the line charge density and inversely proportional to B. Even though $V_t=0$ in the simulations for Fig. 7, the peaks are not exactly centered at the resonance positions $m_1/m_2=0.5$ and 0.9. The resonance peaks are centered at higher m_1/m_2 positions with larger shifts for smaller magnetic field values. These shifts are due to the space charge induced frequency shifts which are negative and whose magnitudes are inversely proportional to B. It is likely that for the simple model involving two cylindrical ion clouds the class of resonances Eq. (25) coupling cyclotron and magnetron modes is not too important for FT-ICR. Only the low order resonances ($n<10$) show significant effects in the numerical simulations. However, in experiments employing high field magnets these resonances are probably avoided due to their narrow widths and sensitive positional dependences on experimental parameters such as trapping potential. Future experiments are required to determine their actual importance to mass spectrometry.

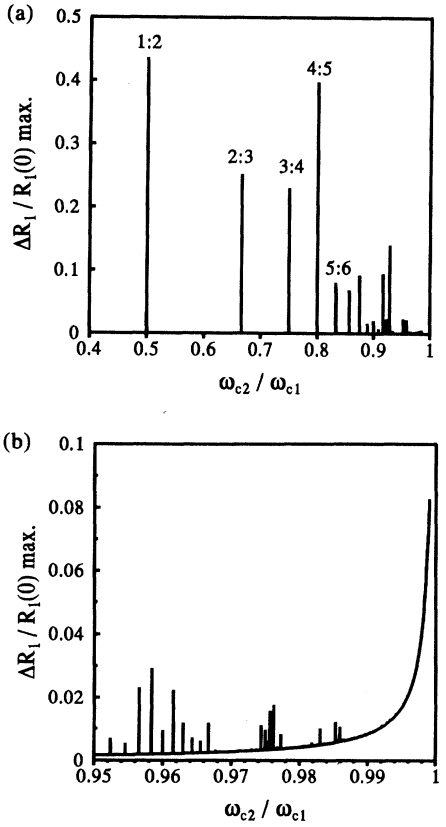

FIG. 5. Numerical simulations of the dependence of the maximum variation in cyclotron radius as a function of cyclotron frequency ratio. Conditions are $m_2=100$ u, $0.999>m_1>0.4$ with all other parameters the same as in Fig. 4.

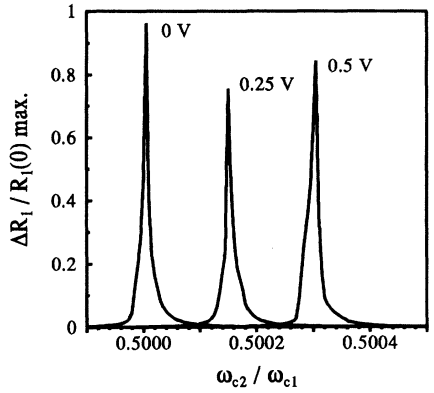

FIG. 6. Dependence of the position of the primary 1:2 resonance on trapping voltage. Three different trapping voltages (0, 0.25, and 0.5 V) are shown and the ICR trap is assumed to be cubic geometry. Note that there is close to a 100% variation in cyclotron radius at the resonance maximum. All other parameters are the same as used in Fig. 4.

D. $\Delta\omega_c$ modulation and phase-locked motion

The cyclotron radii and phases are modulated due to the effective time dependence of the interaction each ion cloud experiences as they pass one another during their cyclotron trajectories. The frequency of the perturbing force is evidently $\sim\Delta\omega_c$, the difference in cyclotron frequency for the two ion clouds. Amplitude modulation

arising from $\Delta\omega_c$ modulation is clearly visible in Fig. 5(b) as the roughly exponential increase in cyclotron radius variation with increasing ω_{c2}/ω_{c1}. When $\langle d\gamma/dt \rangle \approx 0$ corresponding to $\Delta\omega_c \approx 0$, a resonance condition is satisfied, which we call the phase-locking resonance. In order to understand the origin of $\Delta\omega_c$ modulation in the two ion cloud model recall that each cloud experiences a Coulomb force from the other cloud resulting in an $\vec{E}\times\vec{B}$ drift which is in addition to the cyclotron motion around the ICR trap center.

Earlier work has shown [40] that frequency (or phase) modulation results in spectral sidebands with spacing at the cyclotron frequency difference; however, in that study the cyclotron radii were held constant. A quantitative description of $\Delta\omega_c$ modulation requires including the time variation of the cyclotron radii as well as the phases in the analysis. In any case the $\vec{E}\times\vec{B}$ drift, where $\vec{E}$ is due to the interaction between ion clouds, is the origin of the phase-locking phenomenon. It is impossible to predict phase locking without consideration of the time dependence of the cyclotron radii.

Phase locking between two ion clouds in a FT-ICR mass spectrometer has recently been observed [41,42]. In addition, Naito and Inoue [42] have developed a theory

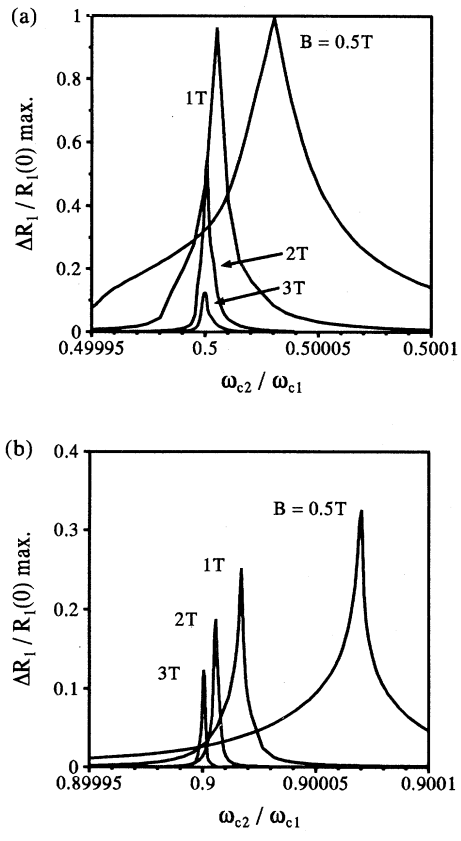

FIG. 7. Dependence of the maximum variation in R_1 as a function of magnetic field at the (a) 1:2 ($n=1$) resonance; (b) 9:10 ($n=9$) resonance. The magnetic field values of $B=0.5$, 1, 2, and 3 T are shown. $m_2=100$ u while m_1 is varied. All other conditions are the same as given in Fig. 4.

for cyclotron phase locking based on the point charge model. We shall demonstrate below that, contrary to the theory of Naito and Inoue, the phase-locking threshold is strongly dependent on the initial separation distance of the two ion clouds. In addition, we show that any theory which does not include the finite diameter of the ion cloud is in error from a quantitative point of view. The finite size of the ion cloud reduces the onset of phase-locking compared to the simple point charge model. Our predictions are supported by comparison of exact numerical calculations with previously published experimental data.

Cyclotron phase locking is just one example of a general and pervasive phenomenon among coupled nonlinear oscillators. Phase locking (alternatively called mode locking, frequency locking, frequency entrainment, or simply synchronization) occurs in electrical, mechanical, acoustical, and control systems [62,63]. The principal system requirements [62,63] appear to be two nonlinearly coupled oscillators whose natural frequencies are close to a small integer fraction, such as 1:1. The earliest scientific observation [63,64] of phase locking was by Huygens in 1673, who described how two pendulum clocks with slightly different natural frequencies hanging back to back on the same thin wall would eventually synchronize their motions. Finally, phase locking is observed in rf Paul traps as well as in Penning traps [59,65].

Cyclotron phase locking arises when the $\vec{E}\times\vec{B}$ drift dynamics due to the Coulomb interaction between ion clouds dominates the cyclotron dynamics. In particular, if the two ion clouds rotate about each other in a time which is shorter than the time required for the two clouds to traverse the same distance due to just their cyclotron motion, the ion clouds may phase lock [56]. Figure 8 shows cyclotron radii, β, γ and separation distance for two cylindrical ion clouds with $N_1=N_2$, $m_1=99.99$ u, $m_2=100.00$ u, $B=1$ T, $\rho_c=0.1$ cm, and $\Delta\omega_c=(2\pi)15.358$ Hz, at three different numbers of ions.

The ion clouds are assumed initially completely overlapping ($\gamma_0=0$) which follows from experimental considerations. If two closely spaced m/Z ion clouds are excited to the same cyclotron radius in a time much shorter than $2\pi/\Delta\omega_c$ then immediately after excitation the ion clouds have the same initial cyclotron phases; thus $\gamma_0=0$. These considerations disregard Coulomb interactions. The phase locking is actually more prominent at smaller cyclotron radii since the ion clouds experience a greater time-averaged interaction force in this case. If the ion clouds are phase locked after excitation, the clouds were likely phase locked before excitation. Therefore $\gamma(0)\approx 0$ immediately after the excitation event.

The plots for R_j show significant modulation. In going from $N_1=N_2=10\times10^3$ ions to 25×10^3 ions the modulation amplitude increases significantly. In going from 25×10^3 to 30×10^3 ions the modulation amplitude decreases while the frequency of the modulation increases. The ion clouds are phase locked when there are $N_1=N_2=30\times10^3$ ions. This is most evident in Fig. 8(d) where the ion cloud separation distance r_{12} remains a small value. If Coulomb interactions are neglected then 2 cm $> r_{12} > 0$. In Fig. 8(b) one observes that the frequency

shift is negative for both ion clouds when $N_1=N_2=10\times10^3$. However, at 25×10^3 ions, ion clouds 2 and 1 experience a positive and negative frequency shift, respectively, indicating that the cyclotron frequency difference between the two clouds is beginning to decrease. At phase locking ($N_1=N_2=30\times10^3$) the frequency shifts are even larger in magnitude. When phase locking occurs, we have the condition that the average value of γ is zero. Using Eq. (11) and the relation between frequency shifts and β_j (numerically, frequency shifts are the slope of a linear variation in β_j as a function of time), the phase-lock condition is

$$\langle\dot{\gamma}\rangle=\omega_{+1}-\omega_{+2}+\langle\dot{\beta}_1\rangle-\langle\dot{\beta}_2\rangle=0\ , \tag{26}$$

where $\langle\ \rangle$ denotes the time average over a long observation period. Figure 8(c) plots $\gamma(t)$ demonstrating that the phase-lock condition $\langle\dot{\gamma}\rangle=0$ is satisfied for $N_1=N_2=30\times10^3$ ions. In ordinary motion when the ion clouds are not phase locked, the magnitude of the phase $\gamma(t)$ increases indefinitely. For phase-locked ion clouds, $\gamma(t)$ oscillates about $\gamma=0$.

Since two ion clouds which are at or near the phase-locking threshold are initially overlapping ($\gamma_0=0$), quantitative agreement with experiment requires a theory which includes the nonzero radius of experimentally realistic ion clouds. While the finite radius of actual ion clouds is easily included in computer simulations, it is much more difficult to do so in deriving an analytical theory for phase locking. On the other hand, we shall demonstrate that it is possible to derive simple analytical phase-locking thresholds for the point and line charge models. The phase-locking thresholds for the simple point and line charge models are strongly dependent upon the initial phase separation γ_0. When the finite size ion clouds are initially overlapped, the point and line charge model results are inappropriate for predicting the phase-locking threshold for finite radius ion clouds. However, two ion clouds which are not partially overlapped initially and are at or near phase locking tend to avoid each other. For this situation, the point and line charge model results should be close to the phase-locking thresholds for realistic clouds. The experimentally relevant case when the clouds are initially overlapping ($\gamma_0\ll1$) is treated by assuming that the point or line charge model results are approximately correct for actual ion clouds assuming that the initial separation distance s between point or line charges is replaced by an effective separation distance s_{eff} which is proportional to the ion cloud radius. The proportionality constant between s and

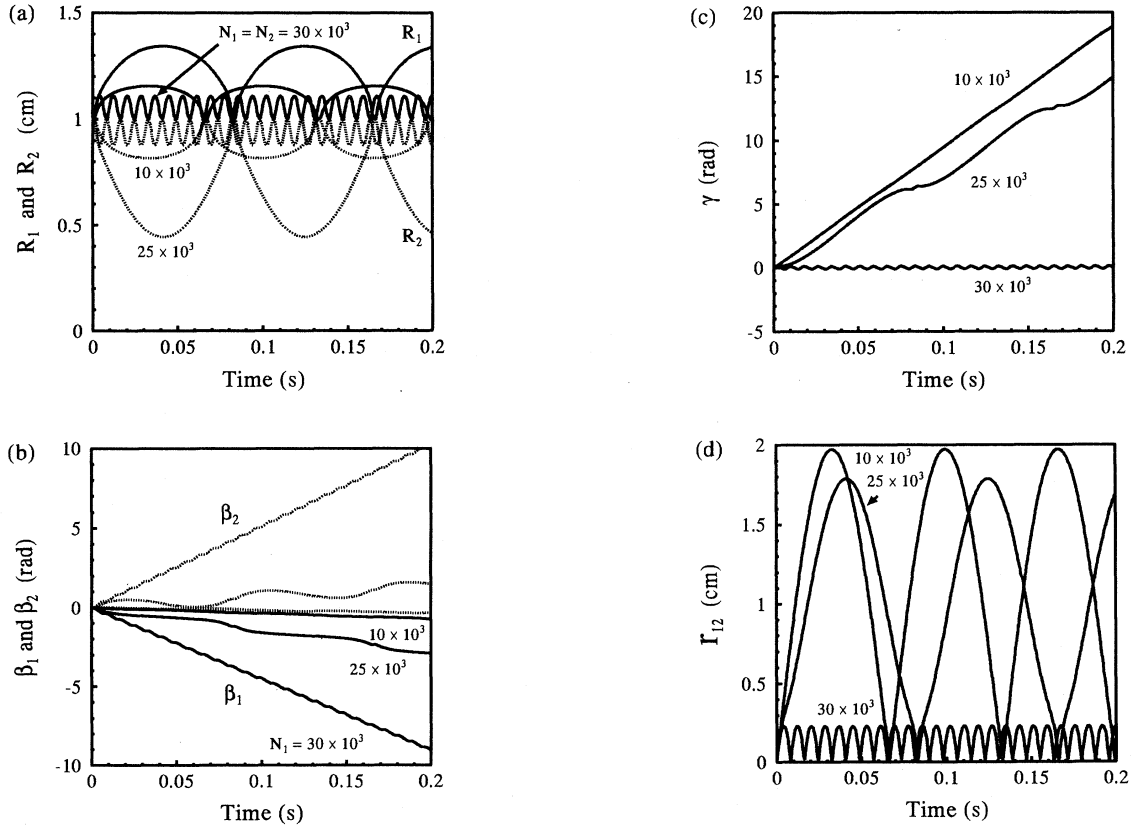

FIG. 8. Numerical simulations using cylindrical ion clouds ($\rho_c=0.1$ cm and $L=5$ cm) before and after the phase-locking threshold. Three different ion populations are shown: $N_1=N_2=10\times10^3$, 25×10^3, and 30×10^3. (a) R_1 and R_2 as a function of time. R_1 and R_2 oscillate above and below, respectively, their initial values. (b) Cyclotron phase $\beta_j(t)$. (c) Cyclotron phase separation $\gamma(t)=(\omega_{+1}+\omega_{+2})t+\beta_1-\beta_2$. (d) $r_{12}(t)$, the separation distance between the ion cloud centers. Conditions include $B=1$ T, $m_1=99.99$ u, $m_2=100$ u, $q_1=q_2=e$, $V_t=0$ V, $R_{10}=R_{20}=1$ cm, $\beta_{10}=\beta_{20}=0$ rad.

s_{eff} is determined by comparing analytical point or line charge model phase-locking thresholds with numerical simulations using spherical or cylindrical ion clouds.

Equations (10) and (14) can be considerably simplified. First of all, the constant of motion Eq. (21) can be used to eliminate R_2. Second, since there is only a single phase variable γ on the right-hand sides of Eq. (14), the two equations for β_1 and β_2 can be replaced by a single equation for γ by using Eq. (11). One can show [66] using methods similar to those in Ref. [67] that a second constant motion exists for the line and point charge models when $q_1N_1=q_2N_2$, the Hamiltonian H. From Eq. (10) for the line charge model, the Hamiltonian for the special case when both line charges have the same line charge density q_1N_1/L and the same initial cyclotron radius R_c is

$$H=\Delta\omega_c R_1^2-\frac{q_1N_1}{2\pi\varepsilon_0 BL}\ln\left\{1-\cos(\gamma)\left[2\left[\frac{R_1}{R_c}\right]^2-\left[\frac{R_1}{R_c}\right]^4\right]^{1/2}\right\}, \tag{27a}$$

where we have used the conditions $R_1(0)=R_2(0)=R_c$ and $q_1N_1=q_2N_2$. Since H is a constant of motion, the line charge is constrained to a trajectory of constant H. The Hamiltonian for the point charge model, Eq. (14), using these parameters is

$$H=\Delta\omega_c R_1^2+\frac{q_1N_1}{2\pi\varepsilon_0 B}\times\frac{1}{[2R_c^2-2\cos(\gamma)\sqrt{2R_c^2R_1^2-R_1^4}\,]^{1/2}}. \tag{27b}$$

Equation (27) gives some insight into the phase-locking condition and can be used to calculate graphically the exact phase-locking threshold without solving any differential equations. Solving the line charge model Hamiltonian, Eq. (27a), for $\cos\gamma$ yields

$$\cos\gamma=\frac{1}{\sqrt{2(R_1/R_c)^2-(R_1/R_c)^4}}\times\left\{1-\exp\left[\frac{2\pi\varepsilon_0 BL}{q_1N_1}(\Delta\omega_c R_1^2-H_0)\right]\right\}, \tag{28a}$$

where $H_0=H(R_1=R_c,\ \gamma=\gamma_0)$ is calculated from Eq. (27a). Similarly, for the point charge model

$$\cos\gamma=\frac{1}{R_1\sqrt{2R_c^2-R_1^2}}\times\left\{R_c^2-2\left[\frac{q_1N_1}{4\pi\varepsilon_0 B(H_0-\Delta\omega_c R_1^2)}\right]^2\right\}. \tag{28b}$$

A necessary condition is that $R_1<\sqrt{2}R_c$ which follows from either Eqs. (21) or (28). In addition the choice of allowed R_1 in Eq. (28) is restricted since $-1\le\cos\gamma\le+1$ must also be satisfied. Equation (28) allows one to obtain exact phase-locking thresholds by a simple graphical technique. Figure 9 plots $\cos\gamma$ versus R_1 obtained directly from Eq. (28) with the same parameters as in Fig. 8 at initial phase separation $\gamma_0=\pi/10$. As a demonstration, consider the results in Fig. 9(b) for the point charge model calculated directly from Eq. (28b). Three different numbers of ions ($N_1=N_2$) are shown. For $N_1=11\times10^3$ ions the R_1 vs $\cos\gamma$ curve intersects $\cos\gamma=1$ at one point then continues to $\cos\gamma=-1$ (not shown) for increasing R. Since all possible values of $\cos\gamma$, and hence γ, are allowed for this case, the two point charges are not phase locked. On the other hand, when $N_1=12.5\times10^3$ and $N_1=14\times10^3$ the curves intersect $\cos\gamma=1$ at two points. Since $R_1(0)=1.0$ cm and $\cos\gamma>1$ is not allowed, the allowed values for $R_1(t)$ are confined to within the points of intersection where $\cos\gamma=1$. As seen from Fig. 9, the range of $\cos\gamma$ values is restricted to approximately $0.95<\cos\gamma<1.0$. Since the maximum variation in $\cos\gamma$ does not cover the entire range of $-1\le\cos\gamma\le+1$, the two ion clouds are phase locked. Results for the line charge model are shown in Fig. 9(a) using the same conditions as for the point charge model. For this case the line charges are locked when $N_1=60\times10^3$ but not locked when $N_1=55\times10^3$ ions.

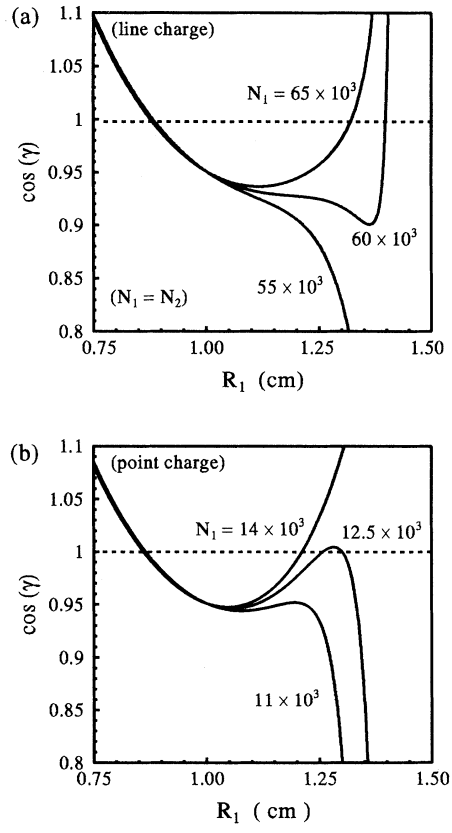

FIG. 9. $\cos(\gamma)$ vs cyclotron radius R_1 calculated from Eq. (28) for the (a) line charge and (b) point charge models. The dynamics are constrained to within the region $1>\cos\gamma>-1$ and $R_1<\sqrt{2}R_c$. Conditions include $B=1$ T, $m_1=99.99$ u, $m_2=100.00$ u, $q_1=q_2=e$, $N_1=N_2$, $R_{10}=R_{20}=R_c=1$ cm, $\gamma_0=0.1\pi$.

It is also possible in principle to derive exact analytical expressions for the cyclotron phase-locking thresholds from Eq. (28). As demonstrated for the conditions used in Fig. 9, the point or line charges are phase locked if $\cos\gamma=1$ at two points subject to the constraint Eq. (21). If the initial cyclotron radii are equal to R_c, then the imposed constraint is that the maximum allowable $R_1=\sqrt{2}R_c$. We take a much simpler though approximate approach here. As observed from Fig. 9, for the case of equal initial cyclotron radii, the two line or point charges are phase locked if $\cos\gamma>0$ at the point $R_1=\sqrt{2}R_c$. Using this approach, from Eq. (28a) two line charges with equal line charge density q_1N_1/L and equal initital cyclotron radii R_c, which are initially separated by γ_0 in a magnetic field B, are phase locked if their cyclotron frequency difference satisfies

$$|\Delta\omega_c| < \left| \frac{q_1N_1}{2\pi\varepsilon_0 BLR_c^2} \ln(1-\cos\gamma_0) \right| . \tag{29a}$$

Similarly, from Eq. (28b) two point charges, each containing charge q_1N_1, are phase locked if

$$|\Delta\omega_c| < \left| \frac{q_1N_1}{2\sqrt{2}\pi\varepsilon_0 BR_c^3} \left[1-\frac{1}{\sqrt{1-\cos\gamma_0}} \right] \right| . \tag{29b}$$

These analytical predictions are compared to numerical solutions of Eqs. (10) and (14) in Fig. 10 demonstrating excellent agreement for most values of γ_0. The agreement is not as good in the region $\gamma_0 \ll 1$. A kinematic model is used below to derive approximate phase-locking thresholds for this special case which is valid if the initial separation distance $s \ll R_c$.

We find that when $\gamma_0<\pi/2$, if phase locking occurs, then $0<\cos\gamma<1.0$. When $\gamma_0>\pi/2$ then $-1.0<\cos\gamma<0$ if the point charges phase lock. However, if $\gamma_0=\pi/2$ which implies $\cos\gamma_0=0$, we find that phase locking never occurs. In most experiments the typical initial condition is $\gamma_0 \ll 1$. Below we derive a simple and surprisingly accurate kinematical model for phase locking valid when $\gamma_0 \ll 1$. By comparing model calculations for the point and line charge models ($\rho_c=0$) with results from numerical simulations for spherical and cylindrical charge models ($\rho_c>0$), the point and line charge models are parametrized to include finite size ion clouds.

Consider the case $m_2>m_1$, $q_1=q_2$, $N_1=N_2$, $R_{10}=R_{20}=R_c$, and initial phase separation $\gamma(0)=\gamma_0$. In a frame of reference moving with m_2, and ignoring Coulomb interactions m_1 approaches m_2 with a velocity $v_1=R_c\Delta\omega_c$. Ion cloud m_1 catches up to m_2 in a time $\tau_{\rm rel}=\gamma_0/\Delta\omega_c$. When Coulomb interactions are included, both m_1 and m_2 receive an additional cyclotron velocity component equal to $\vec{v}_d=-(\vec{E}\times\vec{B})/B^2$ (see the Appendix). Under most conditions, the net effect of v_d is to introduce a slight variation in the circular cyclotron orbit such that the two ion clouds tend to move out of each other's way since $\vec{E}_{12}=-\vec{E}_{21}$. During locked motion, the ion clouds revolve around each other due to $\vec{E}\times\vec{B}$ drift with a period of oscillation on the order of $\tau_d=\pi sB/E$, where s is the initial separation distance between the two ion clouds. The initial separation is related to γ_0 by $s^2=R_c^2(2-2\cos\gamma_0)$, assuming that both ion clouds have the same initial cyclotron radius. When the relative cyclotron motion is included and $\tau_d>\tau_{\rm rel}$, the ion clouds likely rotate in perturbed (modulated) cyclotron orbits with slightly shifted cyclotron frequencies. However, if $\tau_d<\tau_{\rm rel}$, then the ion clouds' $\vec{E}\times\vec{B}$ rotation frequency is greater than the cyclotron frequency difference. For this case, the ion clouds may rotate completely around each other due to $\vec{E}\times\vec{B}$ drifts before the ion clouds can pass each other due to their cyclotron frequency difference. The kinematic condition $\tau_d<\tau_{\rm rel}$ defines the cyclotron phase-locking condition

$$\Delta\omega_c < \frac{\gamma_0 E}{\pi sB} , \tag{30}$$

where E is given by Eqs. (9b) and (13b) for the point and

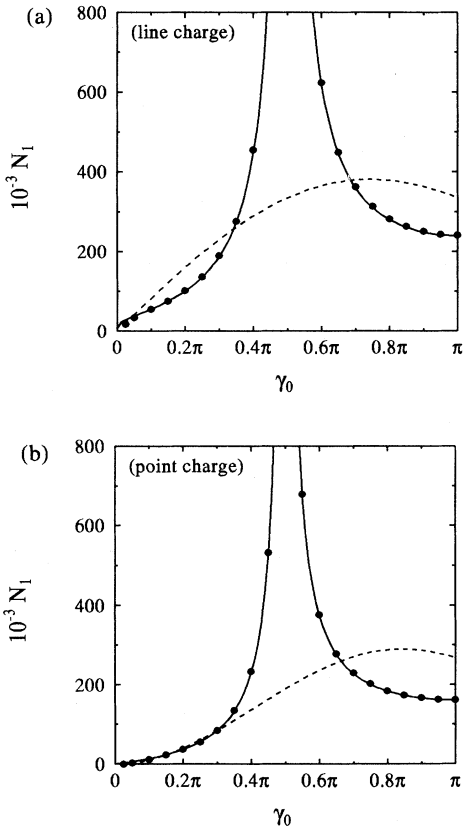

FIG. 10. Comparison between numerical and analytical phase-locking thresholds as a function of initial angular separation γ_0 between ion clouds for (a) the line charge model and (b) the simple point charge model. The numerical results are shown as solid circles. Predictions from Eq. (29) and the kinematic model Eq. (30) are displayed as solid and broken lines, respectively. For the numerical simulations $\rho_c=0$ is used. The numerical phase-locking threshold is calculated by varying the total number of ions, $N_1+N_2=2N_1$, until the phase-lock condition Eq. (26) is satisfied. Equation (26) is equivalent to the statement that the perturbed cyclotron frequencies are equal for the two ion clouds. Other conditions are $R_{10}=R_{20}=1$ cm, $B=1$ T, $m_1=99.99$ u, $m_2=100.00$ u, $L=5$ cm, $q_1=q_2=e$, $N_1=N_2$.

line charge models, respectively, with $r=s$ in those expressions. If the cyclotron radius R_c is much greater than the initial separation s, then $s \approx \gamma_0 R_c$ and Eq. (30) reduces to $\Delta\omega_c < E/(\pi R_c B)$. Assuming that $R_c \gg s$, the phase-locking condition for the point charge model is

$$\Delta\omega_c < \frac{N_1 q_1 + N_2 q_2}{4\pi^2 \varepsilon_0 B R_c s_{\text{eff}}^2} . \tag{31}$$

An effective initial ion cloud separation s_{eff} is substituted for s in anticipation of including finite ion cloud size ($\rho_c > 0$) effects. For the simple point charge and line charge models $s_{\text{eff}}=s$. Intuitively, for finite size ion clouds which are initially completely overlapped, one expects that s_{eff} is on the order of ρ_c. Similarly, for the line charge model when $R_c \gg s$, Eq. (30) reduces to

$$\Delta\omega_c < \frac{N_1 q_1 + N_2 q_2}{2\pi^2 \varepsilon_0 L B R_c s_{\text{eff}}} . \tag{32}$$

In Eqs. (31) and (32) the two ion clouds are now allowed to have different charges and numbers of ions. This is an approximation based on the results of numerical simulations. Equations (31) and (32) are accurate when $q_1 N_1 = q_2 N_2$ and $\rho_c \ll R_c$. For example, using the same parameters as in Fig. 9, we find that two cylindrical ion clouds phase lock with only 15% more (27% less) ions when the slower (faster) ion cloud contains $2N-1$ ions while the faster (slower) cloud contains just one ion, compared to the case when both clouds contain N ions each. Similar results are obtained for spherical ion clouds. These phase-locking thresholds are based on kinematic considerations rather than the solution of the dynamical equations of motion. Their validity needs to be compared with numerical solutions of the exact equations of motion. Equation (30) is derived assuming that the $\vec{E}\times\vec{B}$ drift results in a circular trajectory of each ion cloud around one another, if the ion clouds have equal total charges. This is unlikely due to the additional circular cyclotron trajectory. However, if $R_c \gg s$, then at phase locking the cyclotron trajectory of one ion cloud as seen by the other cloud is nearly linear over one period of the $\vec{E}\times\vec{B}$ drift rotation. When $R_c \gg s$, Eqs. (31) and (32) are expected to provide an adequate prediction of the phase-locking threshold for the simple point charge and line charge models. Additional numerical simulations employing finite radius ion clouds have been carried out which verify the parameter dependences predicted in Eqs. (31) and (32) for the limits $R_c \gg \rho_c$ and $\gamma_0=0$.

Figure 10 compares results from numerical simulations (solid circles) with analytical predictions from Eq. (29) (solid line) and the kinematic approximation Eq. (30) (broken line) for phase-locking thresholds; the number of ions $N_1 (N_1=N_2)$ in the point charge or line charge required to produce phase-locking as a function of the initial phase separation angle γ_0. The conditions used are $\rho_c=0$, $N_1=N_2$, $R_{10}=R_{20}=1$ cm, $B=1$ T, $m_1=99.99$ u, $m_2=100.00$ u, and $q_1=q_2=e$. For these parameters, $\Delta\omega_c=(2\pi)15.358$ Hz. Figure 10 shows a strong dependence of the phase-locking threshold on the initial angular separation between ion clouds γ_0. Qualitatively, since γ_0 and s are related, and the drift velocity direction is perpendicular to $\vec{E}$, larger values for s tend to require a greater number of ions to induce phase locking. The ion clouds remain farther apart on average over time for larger initial separation s than smaller initial separation distance. The analytical phase-locking results, Eq. (29), are seen in Fig. 10 to agree very well with the numerical simulations for most γ_0 values. One observes that the kinematic results are in quantitative agreement with the numerical simulations only for small γ_0, corresponding to $s \ll R_c$, and there is dramatic disagreement when $\gamma_0=\pi/2$. Numerical simulations and Eq. (29) show that when $\gamma_0=\pi/2$ the ion clouds do not phase lock at any number of ions. However, only the case $\gamma_0 \ll 1$ is likely of experimental significance. In this regime the numerical and kinematic calculations are in reasonable agreement. Additional numerical simulations demonstrate that in the limits $\gamma_0 \ll 1$ and $s \ll R_c$ the number of ions required to phase-lock two line charges or two point charges follows the parameter dependences predicted by the kinematic results, Eq. (31) and (32), respectively.

The ion clouds are likely initially overlapped ($\gamma_0=0$) at or near the phase-locking threshold. This follows from the $1/R_c$ dependences in Eqs. (31) and (32) which predict that ion clouds are more likely to phase lock at smaller cyclotron radii. Assuming that the ion clouds, before cyclotron excitation, originate from a single larger ion cloud aligned along the z axis, then if the ion clouds are phase locked after excitation they probably were phase locked before cyclotron excitation. These considerations indicate that $\gamma_0=0$ for finite size ($\rho_c > 0$) ion clouds at or near the phase-locking threshold. Simple models which assume $\rho_c=0$ such as the point charge or line charge models are incompatible with the initial condition $\gamma_0=0$ (which implies $s=0$), since for this case Eqs. (31) and (32) predict that, no matter how little charge or how large $\Delta\omega_c$, the two ion clouds are phase locked.

However, if the finite diameter of the ion clouds is included, then the clouds phase lock only if a reasonably large number of ions is present or if $\Delta\omega_c$ is below a particular value, even when the ion clouds are initially overlapped. The finite size effect is taken into account within Eqs. (31) and (32) by postulating that s_{eff} is an effective initial separation distance which is on the order of the ion cloud radius ρ_c. While Eqs. (31) and (32) are based on the point charge and line charge models, respectively, we propose that they are also correct results for initially overlapped finite diameter ion clouds as long as s is replaced by s_{eff}.

The effective initial cloud separation s_{eff} is calculated by parametrization of Eqs. (31) and (32) with exact numerical simulations using finite size ion clouds. Figure 11 shows results from numerical integration of the exact equations of motion (solid lines) and fits to Eqs. (31) and (32) (broken lines) as a function of the ion cloud diameter. The cylindrical and spherical charge model numerical results are fitted by functions which are linear and quadratic, respectively, in ρ_c which follow from Eqs. (31) and (32). The good fits seen in Fig. 11 support our assumption that s_{eff} is proportional to ρ_c. We obtain numerically

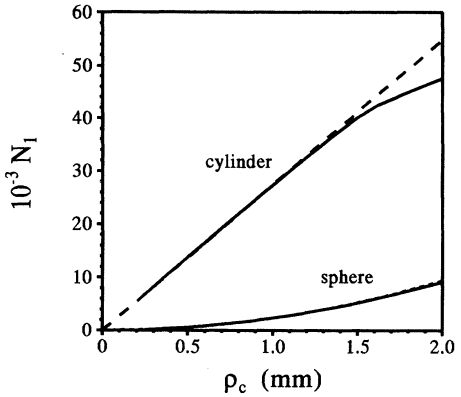

FIG. 11. Numerically calculated phase-locking thresholds (solid lines) for different radius ion clouds when $N_1 = N_2$ and the ion clouds are initially completely overlapping. The top and bottom curves are results for cylindrical and spherical ion clouds, respectively. The broken lines are best fits of Eqs. (31) and (32) to the numerical results assuming that s_{eff} is proportional to ρ_c. Conditions are the same as in Fig. 10.

$$s_{\text{eff}} \cong \begin{cases} 1.50\rho_c & \text{(spherical charge model)} \quad (33a) \\ 1.04\rho_c & \text{(cylindrical charge model)} \; . \quad (33b) \end{cases}$$

With Eqs. (33a) and (33b) in Eqs. (31) and (32), respectively, the simple point and line charge models give approximate phase-locking thresholds for finite diameter ion clouds which are initially completely overlapped. The effective separation s_{eff} is on the order of ρ_c, as expected. In addition, as seen from Fig. 11, spherical ion clouds phase lock with far fewer ions in general for the range of diameters shown than cylindrical ion clouds. For example, 0.1 cm radius spherical ion clouds phase lock with about $\frac{1}{10}$ the number of ions required to phase-lock long cylindrical ion clouds.

Huang *et al.* [41] have carried out careful FT-ICR experiments with two closely spaced m/Z ion clouds, demonstrating cyclotron phase locking for a sufficiently large ion population. In addition, they have observed that the measured abundances by FT-ICR do not reflect the true ratio just before phase locking. The lower m/Z (higher ω_c) ion cloud has a preferentially enhanced detected signal compared to the higher m/Z ion cloud. In Ref. [41] CO^+ (m/Z 27.9944 u) and $N_2{}^+$ (m/Z 28.0056 u) are studied in two different ratios as a function of total ion population. In one set of experiments the ratio $CO{:}N_2 = 1{:}1$ was measured at three different ion populations. Also, the ratio $CO{:}N_2 = 4{:}11$ was studied at four different populations. We shall use these data as a test case for our theoretical model.

The experimental conditions listed in Ref. [41] include $V_t = 1$ V, $B = 0.7$ T, and a cubic ICR trap of length $L = 5$ cm. Neither the postexcitation cyclotron radius nor the electron beam diameter were reported in [41]. Therefore we present predicted results for two different cyclotron and ion cloud radii which are considered reasonable.

For simplicity, the smallest and highest m/Z ion clouds are referred to as m_1 and m_2, respectively. The cyclotron frequency difference $\Delta\omega_c = (2\pi)154.03$ Hz. The ion clouds are assumed to initially have the same cyclotron radius and phase. Hence the ion clouds are initially completely overlapping. With these initial conditions, the spherical charge model, Eqs. (31) and (33a), and the cylindrical charge model, Eqs. (32) and (33b), are used to predict the minimum total number of ions $N_t = q_1 N_1 + q_2 N_2$ which produces cyclotron phase locking. With $R_c = 1.0$ cm and $\rho_c = 0.1$ cm, the spherical and cylindrical charge models predict $N_t = 3.3 \times 10^4$ and 3.8×10^5 ions, respectively, for the phase-locking threshold. If $R_c = 2.0$ cm and $\rho_c = 0.2$ cm, the spherical and cylindrical charge models predict $N_t = 2.6 \times 10^5$ and 1.5×10^6 ions, respectively. Experimentally, Huang *et al.* [41] find that for $m_1{:}m_2 = 1{:}1$ the ion clouds are phase locked at 1.2×10^6 total ions but not at 6.9×10^5; for the ratio $m_1{:}m_2 = 4{:}11$, the ion clouds are phase locked at 1.4×10^6 ions but not at 6.9×10^5 ions. Our predictions based on the cylindrical charge model are in reasonable agreement with the experimental data. The spherical charge model underpredicts the phase-locking threshold for the given parameters. Initially overlapped charged spheres are much more likely to phase lock than charged cylinders.

The experimental observation [41] of the variation in isotope ratios which favors a stronger FT-ICR signal for m_1 (CO^+) than m_2 ($N_2{}^+$) can be explained from either simple kinematics or the cyclotron equations of motion. If both ion clouds have the same initial cyclotron radius and are initially overlapping, then after a short time the faster ion cloud (m_1) has moved slightly ahead of m_2 due to their difference in cyclotron frequency. Each ion cloud also gains an additional velocity component in the $-\vec{E}\times\vec{B}$ direction due to the ion cloud Coulombic interaction. Since $\vec{E}_{12} = -\vec{E}_{21}$ for $N_1 = N_2$, simple geometry shows that m_1 is pushed initially to a larger cyclotron radius while the slower m_2 is pushed to a smaller cyclotron radius. As seen from Fig. 8(a), the faster ion cloud m_1 and slower ion cloud m_2 have cyclotron radii which average over time to greater than and less than, respectively, the initial cyclotron radius. This variation in time-average cyclotron radius increases in magnitude as the two ion clouds approach the phase-locking threshold. Since the detected signal in FT-ICR is approximately proportional to the time-averaged cyclotron radius, the intensity ratio $m_1{:}m_2$ increases as one approaches the phase-locking threshold. The observed variation in intensity ratios is not due to any preferential loss of ions, but rather due to differences in cyclotron radius modulation between the higher and lower m/Z species. The good agreement between model calculations and experimental trends strongly supports our contention that ion clouds near the phase-locking threshold are initially overlapped just after cyclotron excitation. If, for example, the ion clouds initially are π out of phase then the trend in observed ratios is reversed, namely, the faster m_1 has a cyclotron radius which initially decreases while m_2 initially increases.

Additional information concerning trends in frequency shift and cyclotron radius before and after phase locking

is obtained by numerical simulations. Figure 12 displays results of numerical trajectory calculations for two cylindrical ion clouds with parameters corresponding to the experiments of Huang *et al.* [41]. The solid and broken lines are results for m_1 (CO^+):m_2(N_2^+) in ratios of 1:1 and 4:11, respectively. The parameters used in the simulations include $L=5$ cm, $\rho_c=0.1$ cm, $R_1(0)=R_2(0)=1$ cm, and $B=0.7$ T. The ion clouds are initially overlapped. Figure 12(a) shows the maximum and minimum variation in cyclotron radius for m_1 and m_2, respectively. One observes that as the total number of ions increases the variation in R_1 and R_2 increases up to the point of phase locking. Figure 12(b) plots differences between shifted cyclotron frequencies and the average unperturbed cyclotron frequency, $(\omega_{c1}+\omega_{c2})/2$. When phase locked, the two ion clouds have the same frequency. For low ion number, both m_1 and m_2 have small negative frequency shifts. However, as the ion population increases and nears phase locking, m_2 eventually has a positive frequency shift. Immediately after phase locking, the ion clouds do not have frequencies which are simply the weighted average of their unperturbed cyclotron frequencies. This is evident from the solid curve in Fig. 12(b) corresponding to N_1:$N_2=1$:1 which does not equal zero relative shift after cyclotron phase locking.

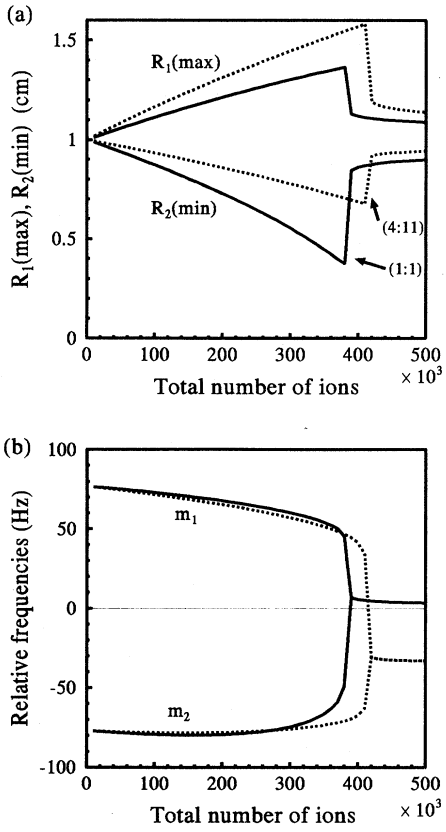

FIG. 12. Numerical simulations using cylindrical ion clouds of the approach to cyclotron phase locking as the total number of ions increases. Ion cloud 1 represents CO^+ ($m_1/Z=27.9944$ u) while ion cloud 2 represents N_2^+($m_2/Z=28.0056$ u). (a) The maximum and minimum values of R_1 and R_2, respectively. (b) Perturbed cyclotron frequencies plotted relative to the average cyclotron frequency. Phase locking occurs when the two perturbed cyclotron frequencies are equal. Two different relative ion populations are shown; $N_1=N_2$ (solid lines) and $N_1=\frac{4}{11}N_2$ (broken lines). Other conditions include $B=0.7$ T, $L=5$ cm, $\rho_c=0.1$ cm, $R_{10}=R_{20}=1$ cm, $\beta_{10}=\beta_{20}=0$.

E. Implications of cyclotron phase locking to mass spectrometry

Cyclotron phase locking sets stringent limits on achievable mass resolution, mass accuracy, and dynamic range in FT-ICR. If too many ions are confined in an ICR trap containing closely spaced m/Z's, a mass spectrum may not be able to resolve the individual masses due to cyclotron phase locking. Assuming that $q_1=q_2$ and $m_1\approx m_2\approx m\gg\Delta m$, where $\Delta m=|m_1-m_2|$, the maximum mass resolution $m/\Delta m$ for spherical ion clouds from Eq. (31) is

$$\frac{m}{\Delta m}<\frac{4\pi^2\varepsilon_0 B^2 R_c s_{\text{eff}}^2}{mN_t}\ , \tag{34}$$

where $N_t=N_1+N_2$; while for the cylindrical charge model

$$\frac{m}{\Delta m}<\frac{2\pi^2\varepsilon_0 L B^2 R_c s_{\text{eff}}}{mN_t}\ . \tag{35}$$

The maximum achievable resolution is inversely proportional to m and the total number of ions, and is directly proportional to B^2. These equations do not imply a restriction on the width of a single mass peak, but rather impose limits on the ability to resolve two adjacent mass peaks. Since phase locking is less likely to occur with cylindrical compared to spherical ion clouds (assuming equal cloud radii and total charges), absolute limits are established for the cylindrical charge model. In addition, we have presented results demonstrating that cylindrical charge models are more appropriate to most FT-ICR experiments than spherical charge models. For these two reasons, further discussions are restricted to only the cylindrical charge model.

In most experiments the closest spaced masses of interest are adjacent isotopes. After phase locking, the isotope peaks are unresolvable in FT-ICR since they have the same detected cyclotron frequencies. Using Eq. (35) with $\Delta m=1$ u gives an estimate of the maximum number of ions $N_{\max}$ in two adjacent ion clouds which can be confined before cyclotron phase locking occurs:

$$N_{\max}\approx 1.1\times 10^{11}\left[\frac{B^2 L R_c \rho_c}{m^2}\right]\ , \tag{36}$$

where B, L, R_c, ρ_c, and m are given in units of T, cm, cm, cm, and u, respectively. One should remember that Eq. (36) assumes that $q_1=q_2$ and $m\approx m_1\approx m_2\gg 1$ u. The most striking feature of $N_{\max}$ is its dependence on $(B/m)^2$. Using typical parameters $L=5$ cm, $R_c=1$ cm, and $\rho_c=0.1$ cm, then $N_{\max}\approx 5.5\times 10^{10}(B/m)^2$ ions. If $B=1$ T and $m=100$ u, $N_{\max}\approx 5.5\times 10^6$ ions. However,

if $B=1$ T and $m=10\,000$ u, then $N_{\max}\approx 550$ ions. These results may help explain the relatively poor performance of the FT-ICR method at very high m/Z (or at low B) when there are too many ions with closely spaced m/Z, an almost inevitable outcome due to the effective isotropic and chemical heterogeneity of these systems.

$N_{\max}$ also sets a limit to the maximum dynamic range achievable in FT-ICR due to cyclotron phase locking. As a limiting criterion, we choose one ion cloud which contains just a single ion while all other ions are in the second ion cloud. The maximum dynamic range for adjacent isotope peaks is then $\sim N_{\max}$.

Mass accuracy is also sacrificed by cyclotron modulation and phase locking. As seen from Fig. 12(b), immediately before the ion clouds phase lock, the frequency shifts have a complicated ion number dependence which is different for each ion cloud. After the two clouds phase lock, an FT-ICR experiment measures a single frequency which is not simply equal to the weighted average of the unperturbed cyclotron frequencies. These results have important implications for FT-ICR experiments on high m/Z biomolecules which typically contain many isotope peaks. For example, mass measurements based on either the monoisotopic peak or the isotope distribution [9] are neither exact nor easily calibrated when the ion clouds are near the phase-locking threshold.

IV. CONCLUSION

This paper investigates the cyclotron dynamics of two Coulombically interacting ion clouds with different m/Z. The models of two interacting point charges and line charges are investigated analytically while exact numerical simulations are used to study spherical and cylindrical ion clouds. These simple models exhibit the most important space charge effects including frequency shifts, amplitude and phase modulation, and cyclotron phase locking.

When the cyclotron frequencies are far apart and incommensurate, the Coulomb interaction primarily results in frequency shifts. For this situation, the cyclotron radii do not vary much from their initial values. Frequency shifts are derived analytically for the simple point charge and line charge models and compared to exact numerical results employing spherical and cylindrical ion clouds. Positive frequency shifts as well as negative frequency shifts are possible for the point and spherical charge models when the two ion clouds have different cyclotron radii. Implications of cyclotron radius dependent, m/Z independent frequency shifts to FT-ICR mass calibration are discussed.

When the cyclotron frequency difference $\Delta\omega_c$ between ion clouds decreases, cyclotron amplitude and phase modulation increases. Angular momentum conservation, Eqs. (21), and energy conservation restrict the allowed variation in cyclotron radius and phase. When the two ion clouds have very close cyclotron frequencies such that $\Delta\omega_c\approx 0$, the ion clouds may phase lock. At cyclotron phase locking the ion clouds no longer possess two independent cyclotron motions, but instead evolve with a single collective cyclotron frequency for the center of mass motion and a $\vec{E}\times\vec{B}$ drift frequency for the relative motion, where $\vec{E}$ is the Coulomb electric field between the two ion clouds. At phase locking the $\vec{E}\times\vec{B}$ cyclotron velocity perturbation entrains one ion cloud to the second ion cloud. Cyclotron phase locking occurs when the $\vec{E}\times\vec{B}$ drift dynamics dominates the relative cyclotron dynamics. Spherical ion clouds are much more likely to phase lock than cylindrical ion clouds due to the generally stronger radial electric field for small diameter spherical clouds compared to long cylindrical clouds with the same diameter and total charge. Our results are compared to previously published experimental data [41]. The present model quantitatively describes the onset of phase locking as well as the general trends in frequency shifts and measured abundances just before phase locking. The implications of cyclotron phase locking for FT-ICR mass spectrometry are discussed and shown to impose additional limits on achievable resolution, mass accuracy, and dynamic range. After phase locking, adjacent isotopes are unresolvable in FT-ICR mass spectrometry since they have the same detected cyclotron frequencies in this case. An estimate of the maximum number of ions $N_{\max}$ in two ion clouds, which are adjacent isotopes, at the phase-locking threshold, Eq. (36), predicts that $N_{\max}$ is proportional to $(B/m)^2$.

ACKNOWLEDGMENTS

We have benefited from extensive discussions with Dr. A. J. Peurrung and Dr. A. L. Rockwood. This work was supported through the U.S. Department of Energy. Pacific Northwest Laboratory is operated by Battelle Memorial Institute through Contract No. DE-AC-06-76RLO-1830.

APPENDIX: GENERALIZED EQUATIONS OF MOTION FOR A SINGLE ION

The motion of a single ion in a constant magnetic field directed along the z axis of an azimuthally symmetric quadrupolar potential is given by [21,23]

$$\begin{aligned} x(t)&=R_+\cos\phi_+ + R_-\cos\phi_- \ , \\ y(t)&=-R_+\sin\phi_+ - R_-\sin\phi_- \ , \\ z(t)&=A_z\cos\phi_z \ , \end{aligned} \tag{A1}$$

where

$$\begin{aligned} \phi_\pm&=\omega_\pm t+\beta_\pm \ , \\ \phi_z&=\omega_z t+\beta_z \ . \end{aligned} \tag{A2}$$

These motions are depicted in Fig. 13 for the x-y plane. The mode amplitudes (R_+,R_-,A_z) and phases $(\beta_+,\beta_-,\beta_z)$ are constants of motion. If the ion experiences an additional perturbation force $\vec{F}$, the trajectory may still be given by Eqs. (A1) and (A2); however, the mode amplitudes and phases now vary with time. One can show that the dynamics in the x-y plane for the perturbed motion is found by solving the amplitude-phase equations of motion [23]

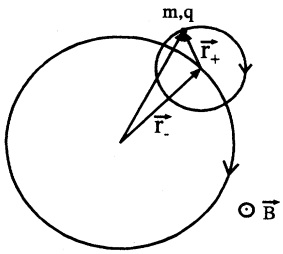

FIG. 13. Geometry of a single $m/q(q>0)$ ion in the $z=0$ plane showing the cyclotron $\vec{r}_+$ and magnetron $\vec{r}_-$ position vectors. The magnetic field B points in the z direction.

$$\begin{aligned}
\dot{R}_+ &= \frac{-1}{m\omega_p}[F_x\sin\phi_+ + F_y\cos\phi_+] , \\
\dot{R}_- &= \frac{1}{m\omega_p}[F_x\sin\phi_- + F_y\cos\phi_-] , \\
\dot{\beta}_+ &= \frac{1}{R_+ m\omega_p}[F_y\sin\phi_+ - F_x\cos\phi_+] , \\
\dot{\beta}_- &= \frac{1}{R_- m\omega_p}[F_x\cos\phi_- - F_y\sin\phi_-] ,
\end{aligned} \tag{A3}$$

where $\omega_p=\omega_+-\omega_-$ and $\vec{F}=(F_x,F_y,F_z)$. Equation (A3) is exact; however, additional flexibility in the choice of the representation for describing the perturbed motion can be derived by rewriting Eq. (A3) in vectorial form. In the new factorial form, the amplitude-phase representation, Eq. (A3), is just a special case. One starts by rewriting Eq. (A1) as

$$\begin{aligned}
x(t) &= x_+ + x_- , \\
y(t) &= y_+ + y_- ,
\end{aligned} \tag{A4}$$

where (x_+,y_+) and (x_-,y_-) are the Cartesian components of the cyclotron and magnetron positions, respectively. By comparing Eq. (A4) with (A1)

$$\begin{aligned}
x_\pm &= R_\pm\cos\phi_\pm , \\
y_\pm &= -R_\pm\sin\phi_\pm .
\end{aligned} \tag{A5}$$

Equation (A5) is identical to a simple polar coordinate transformation (x,y) to $(r,-\phi)$. The negative sign indicates that the ion trajectory rotates in the clockwise direction for a positively charged ion. Taking the time derivative of Eq. (A5) while allowing R and β to be time dependent yields the dynamical equations for $x_\pm$ and $y_\pm$. As an example, consider the x_+ equation,

$$\dot{x}_+ = \dot{R}_+\cos\phi_+ - R_+\dot{\phi}_+\sin\phi_+ . \tag{A6}$$

Substituting Eqs. (A2) and (A3) into Eq. (A6) yields

$$\dot{x}_+ = \omega_+ y_+ - \frac{F_y}{m\omega_p} . \tag{A7a}$$

The results for the other components follow similarly:

$$\dot{y}_+ = -\omega_+ x_+ + \frac{F_x}{m\omega_p} , \tag{A7b}$$

$$\dot{x}_- = \omega_- y_- + \frac{F_y}{m\omega_p} , \tag{A8a}$$

$$\dot{y}_- = -\omega_- x_- - \frac{F_x}{m\omega_p} . \tag{A8b}$$

These equations can be written in vectorial form for the cyclotron and magnetron motion position vectors, $\vec{r}_\pm = x_\pm\hat{i}+y_\pm\hat{j}$. By inspection

$$\dot{\vec{r}}_+ = \left[\omega_+\vec{r}_+ - \frac{\vec{F}}{m\omega_p}\right]\times\hat{k} , \tag{A9a}$$

$$\dot{\vec{r}}_- = \left[\omega_-\vec{r}_- + \frac{\vec{F}}{m\omega_p}\right]\times\hat{k} . \tag{A9b}$$

Equation (A9) is the general expression for the cyclotron and magnetron position vectors. Their solution completely solves the perturbed ion motion in the x-y plane. The amplitude-phase representation, Eq. (A3), is a special case of Eq. (A9). Equation (A9) has a simple physical interpretation in the low m/z limit such that $\omega_+ \gg \omega_z \gg \omega_-$, where $\omega_p\approx\omega_c$, $\omega_+\approx\omega_c$, where $\omega_-\approx\omega_m$. With these approximations we have

$$\dot{\vec{r}}_+ \approx \omega_c\vec{r}_+\times\hat{k} - \frac{\vec{F}\times\vec{B}}{qB^2} , \tag{A10a}$$

$$\dot{\vec{r}}_- \approx \omega_m\vec{r}_-\times\hat{k} + \frac{\vec{F}\times\vec{B}}{qB^2} . \tag{A10b}$$

If the perturbation force $\vec{F}=q\vec{E}$, then the second terms on the right of Eq. (A10) are $\vec{E}\times\vec{B}$ drifts. Equation (A10b) is simply the magnetron drift velocity expression where the first term on the right is the rotation due to the quadrupolar potential and the second term the $\vec{E}\times\vec{B}$ drift. The cyclotron mode equation is very similar except that $\omega_c \gg \omega_m$ and the direction of the $\vec{E}\times\vec{B}$ drift is opposite that for the magnetron mode.

As a further example, consider a polar coordinate system $(R_\pm,\phi_\pm)$ which rotates with the ion, i.e., Eq. (A5). For this case

$$\begin{aligned}
\dot{R}_\pm &= \frac{\pm F_{\phi\pm}}{m\omega_p} , \\
\dot{\phi}_\pm &= \omega_\pm \mp \frac{F_{r\pm}}{R_\pm m\omega_p} ,
\end{aligned} \tag{A11}$$

where $F_{r\pm}$ is the radial and $F_{\phi\mp}$ the azimuthal component of $\vec{F}$, with the azimuthal angle rotating in the clockwise direction.

[1] M. B. Comisarow and A. G. Marshall, Chem. Phys. Lett. **25**, 282 (1974).
[2] M. B. Comisarow and A. G. Marshall, Chem. Phys. Lett. **26**, 489 (1974).
[3] M. V. Buchanan and M. B. Comisarow, in *Fourier Transform Mass Spectrometry: Evolution, Innovation and Applications,* edited by M. V. Buchanan, ACS Symposium Series No. 359 (American Chemical Society, Washington, DC, 1987), Chap. 1.
[4] A. G. Marshall and F. R. Verdun, *Fourier Transforms in NMR, Optical and Mass Spectrometry: A User's Handbook* (Elsevier, Amsterdam, 1990).
[5] A. G. Marshall and P. B. Grosshans, Anal. Chem. **63**, 215A (1991).
[6] R. C. Dunbar, in *FT-ICR/MS: Analytical Applications of Fourier Transform Ion Cyclotron Resonance Mass Spectrometry,* edited by B. Asamoto (VCH, New York, 1991), Chap. 1.
[7] A. G. Marshall and L. Schweikard, Int. J. Mass Spectrom. Ion Processes **118/119**, 37 (1992).
[8] C. L. Holliman, D. L. Rempel, and M. L. Gross, Mass Spectrom. Rev. **13**, 105 (1994).
[9] F. W. McLafferty, Acc. Chem. Res. **27**, 379 (1994).
[10] J. B. Fenn, M. Mann, C. K. Meng, S. F. Wong, and C. M. Whitehouse, Science **246**, 64 (1989).
[11] J. B. Fenn, M. Mann, C. K. Meng, and S. F. Wong, Mass Spectrom. Rev. **9**, 37 (1990).
[12] R. D. Smith, J. A. Loo, R. R. O. Loo, M. Busman, and H. R. Udseth, Mass Spectrom. Rev. **10**, 359 (1991).
[13] R. C. Beavis and B. T. Chait, Anal. Chem. **62**, 1836 (1990).
[14] F. Hillenkamp, M. Karas, R. C. Beavis, and B. T. Chait, Anal. Chem. **63**, 1193A (1991).
[15] J. A. Castoro, C. Köster, and C. L. Wilkens, Rapid Commun. Mass Spectrom. **6**, 239 (1992).
[16] S. Guan and A. G. Marshall, Int. J. Mass Spectrom. Ion Processes (to be published).
[17] M. B. Comisarow, J. Chem. Phys. **69**, 4097 (1978).
[18] L. S. Brown and G. Gabrielse, Rev. Mod. Phys. **58**, 233 (1986).
[19] E. B. Ledford, D. L. Rempel, and M. L. Gross, Anal. Chem. **56**, 2744 (1984).
[20] M. Kretzschmar, Z. Naturforsch. Teil A **45**, 965 (1990).
[21] M. Kretzschmar, Eur. J. Phys. **58**, 240 (1991).
[22] M. Kretzschmar, Phys. Scr. **46**, 544 (1992).
[23] D. W. Mitchell, Int. J. Mass Spectrom. Ion Processes **107**, 417 (1991).
[24] L. Schweikhard and A. G. Marshall, J. Am. Soc. Mass Spectrom. **4**, 433 (1993).
[25] S.-P. Chen and M. B. Comisarow, Rapid Commun. Mass Spectrom. **5**, 450 (1991).
[26] S.-P. Chen and M. B. Comisarow, Rapid Commun. Mass Spectrom. **6**, 1 (1992).
[27] E. A. Cornell, K. R. Boyce, D. L. K. Fygenson, and D. E. Pritchard, Phys. Rev. A **45**, 3049 (1992).
[28] R. C. Dunbar, J. H. Chen, and J. D. Hays, Int. J. Mass Spectrom. Ion Processes **57**, 39 (1984).
[29] Ch. Gerz, D. Wilsdorf, and G. Werth, Nucl. Instrum. Methods Phys. Res. Sect. B **47**, 453 (1990).
[30] M. V. Gorshkov and E. N. Nikolaev, Int. J. Mass Spectrom. Ion Processes **125**, 1 (1993).
[31] M. V. Gorshkov, A. G. Marshall, and E. N. Nikolaev, J. Am. Soc. Mass Spectrom. **4**, 855 (1993).
[32] S. Guan, M. C. Markus, and A. G. Marshall, Anal. Chem. **65**, 3647 (1993).
[33] L. K. Herold and R. T. Kouzes, Int. J. Mass Spectrom. Ion Processes **96**, 275 (1990).
[34] J. B. Jeffries, S. E. Barlow, and G. H. Dunn, Int. J. Mass Spectrum Ion Processes **54**, 169 (1983).
[35] M. Kretzschmar, Z. Naturforsch. Teil A **45**, 979 (1990).
[36] F. Kuhnen, M. Knobeler, and K. P. Wanczek (unpublished).
[37] V. L. Talrose and E. N. Nikolaev, in *Advances in Mass Spectrometry,* edited by J. F. J. Todd (Wiley, New York, 1986), p. 343.
[38] T.-C. L. Wang and A. G. Marshall, Int. J. Mass Spectrom. Ion Processes **68**, 287 (1986).
[39] D. J. Wineland and H. G. Dehmelt, Int. J. Mass Spectrom. Ion Processes **16**, 338 (1975).
[40] C. L. Hendrickson, S. C. Beau, and D. A. Laude, Jr., J. Am. Soc. Mass Spectrom. **4**, 909 (1993).
[41] J. Huang, P. W. Tiedemann, D. P. Land, R. T. McIver, and J. C. Hemminger, Int. J. Mass Spectrom. Ion Processes **134**, 11 (1994).
[42] Y. Naito and M. Inuoue, J. Mass Spectrom. Soc. Jpn. **42**, 1 (1994).
[43] G. T. Uechi and R. C. Dunbar, J. Am. Soc. Mass Spectrom. **3**, 734 (1992).
[44] J. E. Bruce, G. A. Anderson, S. A. Hofstadler, B. E. Winger, and R. D. Smith, Rapid Commun. Mass Spectrom. **7**, 701 (1993).
[45] J. P. Speir, G. S. Gorman, C. C. Pitsenberger, C. A. Turner, P. P. Wang, and I. J. Amster, Anal. Chem. **65**, 1746 (1993).
[46] C. F. Driscoll, in *Low Energy Antimatter,* edited by D. Cline (World Scientific, Singapore, 1986), p. 184.
[47] T. M. O'Neil, in *Non-Neutral Plasma Physics,* edited by C. W. Roberson and C. F. Driscoll, AIP Conf. Proc. No. 175 (AIP, New York, 1988), p. 1.
[48] D. J. Wineland, J. J. Bollinger, W. M. Itano, and J. D. Prestage, J. Opt. Soc. Am. B **2**, 1721 (1985).
[49] L. R. Brewer, J. D. Prestage, J. J. Bollinger, W. M. Itano, D. J. Larson, and D. J. Wineland, Phys. Rev. A **38**, 859 (1988).
[50] J. J. Bollinger, D. J. Heinzen, F. L. Moore, W. M. Itano, D. J. Wineland, and D. H. E. Dubin, Phys. Rev. A **48**, 525 (1993).
[51] J. J. Bollinger, D. J. Wineland, and D. H. E. Dubin, Phys. Plasmas **1**, 1403 (1994).
[52] A. J. Peurrung and R. T. Kouzes, Phys. Rev. E **49**, 4362 (1994).
[53] R. G. Greaves, M. D. Tinkle, and C. M. Surko, Phys. Rev. Lett. **74**, 90 (1995).
[54] R. H. Hunter, M. G. Sherman, and R. T. McIver, Int. J. Mass Spectrom. Ion Processes **50**, 259 (1983).
[55] M. Wang and A. G. Marshall, Anal. Chem. **61**, 1288 (1989).
[56] A. J. Peurrung and R. T. Kouzes, Int. J. Mass Spectrom. Ion Processes (to be published).
[57] A. Cromer, Am. J. Phys. **49**, 455 (1981).
[58] A. D'Innocenzo and L. Renna, Eur. J. Phys. **13**, 153 (1992).
[59] K. Jungmann, J. Hoffnagle, R. G. Devoe, and R. G. Brewer, Phys. Rev. A **36**, 3451 (1987).
[60] D. W. Mitchell, A. L. Rockwood, and R. D. Smith, Int. J. Mass Spectrom. Ion Processes **141**, 101 (1995).
[61] D. W. Mitchell, Int. J. Mass Spectrom. Ion Processes **142**, 1 (1995).
[62] N. Minorsky, *Nonlinear Oscillations* (Van Nostrand, New

York, 1962), Chap. 18.
[63] M. Schroeder, *Fractals, Chaos, Power Laws* (Freeman, New York, 1991), p. 171.
[64] C. Huygens, *Horologium Oscillatorium* (Muget, Paris, 1673).
[65] J. Hoffnagle and R. G. Brewer, Science **265**, 213 (1994).
[66] Transform Eqs. (10) and (14) from variables R and β to canonical variables (J,ϕ) defined by $J=R^2$ and $\phi=\omega_c t+\beta$. The new equations of motion with $N_1q_1=N_2q_2$ obey Hamilton's equations from which the constant of motion H is derived by inspection.
[67] D. W. Mitchell, B. A. Hearn, and S. E. DeLong, Int. J. Mass Spectrom. Ion Processes **125**, 95 (1993).